

pubs.acs.org/Macromolecules Article

Interfacial Compatibilization in Ternary Polymer Nanocomposites: Comparing Theory and Experiments

Shawn M. Maguire,[#] Nadia M. Krook,[#] Arjita Kulshreshtha, Connor R. Bilchak, Robert Brosnan, Andreea-Maria Pana, Patrice Rannou, Manuel Maréchal, Kohji Ohno, Arthi Jayaraman,^{*} and Russell J. Composto^{*}



Cite This: Macromolecules 2021, 54, 797-811



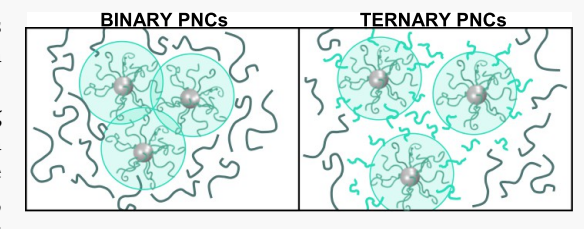
ACCESS

Metrics & More

Article Recommendations

Supporting Information

ABSTRACT: In this work, we examine binary and ternary nanocomposites of poly(methyl methacrylate) grafted silica nanoparticles (PMMA-NP), in poly(styrene-ran-acrylonitrile) (SAN), and poly(methyl methacrylate) matrices as a platform to directly probe governing parameters guiding phase behavior and nanoparticle assembly in composite materials. Through the addition of PMMA matrix chains similar in molecular weight to the grafted PMMA chains and significantly smaller than the SAN matrix chains, we observe increased nanoparticle miscibility in off-critical compositions



due to interfacial segregation of PMMA matrix chains. A simple interfacial model provides a general guideline for predicting the extent of compatibilization. Further insights on compatibilization behavior are provided by polymer particle pair correlation functions and structure factors obtained using polymer reference interaction site model theory calculations as well as polymer concentration profiles from molecular dynamics simulations. This study serves as a guideline to facilitate PNC processing and design of materials for a broad range of technological applications.

■ INTRODUCTION

The ability to control the dispersion state of nanosized inorganic or hybrid fillers in polymer nanocomposites (PNCs) has been a continuous challenge in the development of functional hybrid materials for a wide array of applications. Examples include the addition of rigid polymer nanoparticles (NP) to a liquid or polymer electrolyte for enhanced mechanical modulus without sacrificing ionic conductivity, 1-3 the incorporation of gold nanorods to a polymer matrix for tuning optical absorption and polarization, 4-6 or using polymer-grafted silica nanoparticles to create membranes with controllable separation capabilities. Since the bulk material properties of the composite are directly correlated with the spatial distribution of the nanoparticles within the polymer matrix, 2,8-11 the ability to achieve uniform nanoparticle dispersion through different processing techniques, including self-assembly and external fields, has attracted considerable attention. While there have been significant advances made utilizing these methods, often these are nonequilibrium processes, resulting in composites having metastable morphologies. These kinetically trapped PNCs are therefore unsuitable for applications that operate at high temperatures, which accelerate NP motion and instability, leading to phase separation and degradation. Therefore, finding ways to increase the miscibility windows of these composites at elevated temperatures is enticing for industrial applications that rely on controlled spatial distributions of NPs within the polymer phase.

Previously, it has been shown by Schmitt et al. that a binary PNC system of silica particles grafted with polystyrene (PS) and PMMA ligands with an upper critical solution temperature (UCST) can impart phase behavior comparable to analogous linear polymer blends. 12 However, while the trends in phase behavior between the two systems were similar, the PNC demonstrated increased miscibility and reduced kinetics of domain growth. The apparent increase in miscibility was rationalized as a consequence of a reduced thermodynamic driving force for phase separation by decreasing the number of unfavorable segmental interactions between each ligand. Additionally, the presence of NP cores resulted in a smaller number density of segmental contacts. 12 Similarly, work by Karim and co-workers compared the phase separation behavior of a system of gold nanoparticles grafted with PS (AuPS) inside a PMMA matrix to that of a binary homopolymer blend composed of PS and PMMA.¹³ Comparison of the surface topographies of the two systems revealed a lower interfacial tension between AuPS and PMMA than that in the homopolymer blend. This difference was attributed to the sterically hindered interactions of PMMA matrix chains with

Received: October 16, 2020
Revised: December 16, 2020
Published: January 11, 2021





the chains grafted to the surface of the nanoparticle. Taken together, these studies offer insights into potential routes of facilitating PNC miscibility, specifically, by focusing on the interface between the grafted nanoparticle and matrix.

To probe if the PNC miscibility can be expanded via increased interfacial compatibilization, a polymer system has to be judiciously chosen such that the phase behavior of the homopolymer blend is documented and has an accessible critical point for the tracking of changes in miscibility. The binary homopolymer blend of poly(styrene-ran-acrylonitrile) (SAN, 33 wt % AN) and PMMA has been shown to have an accessible lower critical solution temperature (LCST) of 160 °C that can be tuned through changing the composition of SAN, and to a lesser degree, the molecular weight of the constituents. 14-18 The addition of nanoparticles to the PMMA/SAN blend has been demonstrated as a way to further manipulate both the phase behavior and phase separation temperature of the system. 19-23 While the aforementioned studies focused on UCST PNCs with unfavorable segmental interactions below a critical temperature, the favorable interactions below a critical temperature of the PMMA/SAN blend with the LCST phase behavior allows for direct validation of the proposed interfacial tension and limited segmental interaction theories. Previously, favorable interactions between SAN graft polymers and PMMA matrix polymers in PNCs containing SAN grafted silica nanoparticles have been shown to promote uniform dispersion where chosen design parameters like large particle size, small molecular weight of graft chains, and high molecular weight of matrix chains favored phase separation.²⁴ However, PNCs with graft matrix interactions that follow the LCST phase behavior, exhibiting favorable segmental interactions at low temperatures that become progressively weaker and eventually repulsive as the temperature increases, show a sharp dispersion to aggregation transition on increasing temperature as seen for polystyrene (PS) grafted silica particles in the poly(vinyl methyl ether) (PVME) matrix in past experiments and simulations.²⁵ Accordingly, through the addition of PMMA homopolymer to a binary PMMA-NP/SAN PNC (i.e., LCST composite), the number of favorable segmental interactions between each chemical species can be restored to reduce the thermodynamic driving force for phase separation at high temperatures.

In the present work, we examine binary and ternary nanocomposites of poly(methyl methacrylate) grafted silica nanoparticles (PMMA-NP) mixed with SAN (binary) and PMMA-NPs, SAN, and PMMA homopolymer (ternary) as model systems to directly probe the governing parameters guiding phase behavior and nanoparticle assembly. As-cast PNC films are characterized as a function of nanoparticle loading, revealing well-dispersed NP systems. Phase behavior of the binary and ternary PNC was investigated between 155 and 195 °C and characterized using a combination of cloud point observations, transmission electron microscopy (TEM), and small-angle X-ray scattering (SAXS). For both binary and ternary PNCs, cross-sectional TEM micrographs reveal a threestage transition from discrete to string-like to bicontinuous NP domains with increasing NP loadings when annealed in the two-phase regime. The scattering profiles obtained through SAXS reveal the emergence of two distinct length scales underpinning the binary and ternary PNC phase behavior, specifically, a smaller length-scale feature representing the average center-to-center interparticle distance as well as a

larger length-scale feature representing the scattering between nanoparticle clusters. Modeling of these two scattering features allows for the accurate capture of the phase transition within the binary and ternary PNCs. By compiling the cloud point, TEM, and SAXS results, we demonstrate that the addition of 5 wt % PMMA homopolymer to the binary PNC stabilizes the composite material through directed segregation of PMMA to the PMMA-NP/SAN interface, leading to increased miscibility in off-critical compositions. To explain this compositional dependence, a simple interfacial scaling model is derived, providing a general guideline for predicting the extent of compatibilization. Polymer reference interaction site model (PRISM) theory calculations and molecular dynamics (MD) simulations based on a coarse-grained (CG) model are performed to elucidate the effect of the amount of added PMMA matrix (quantified in terms of volume fraction) on the PNC structure. Experimental plots of the composite structure factors, which show a dispersion to aggregation transition in PNCs on increasing temperature, are compared to particleparticle structure factors obtained using PRISM theory to verify the ability of the CG model to capture experimental phase behavior. Thereafter, MD simulations based on the CG model are used to calculate concentration profiles for graft and matrix polymers in the vicinity of the particle at various PMMA matrix volume fractions. Results from MD simulations show that, when PMMA graft and SAN matrix interactions are unfavorable (at high temperatures), the PMMA matrix concentration increases near the particle surface, suggestive of compatibilization. Further, particle-particle pair correlation functions and particle structure factor plots from PRISM theory show that increased volume fraction of PMMA matrix chains leads to a reduced tendency for aggregation in PNCs at high temperatures.

EXPERIMENTS

Materials. Poly(styrene-ran-acrylonitrile) (SAN, $M_w = 118 \text{ kg/}$ mol, $M_{\rm w}/M_{\rm n}$ = 2.24, $T_{\rm g}$ = 114 °C, containing 33 wt % acrylonitrile) was provided by Monsanto and purified twice by adding a solution of SAN and chloroform (≥99.9%, for HPLC) into methanol (≥99.9%, for HPLC) at a 1:10 volume ratio. After allowing SAN to precipitate for 1 h, the solvent was removed, and the precipitant was dried for 48 h. Once dried, SAN was redissolved in chloroform and precipitated with methanol once more. Poly(methyl methacrylate) (PMMA, $M_w =$ 21 kg/mol, $M_{\rm w}/M_{\rm n}$ = 1.14, $T_{\rm g}$ = 110 °C) was purchased from Polymer Source Inc. and used as received. Silica nanoparticles (15 nm in diameter) grafted with PMMA brushes, denoted as PMMA-NPs, were prepared using surface-initiated atom transfer radical polymerization.²⁶ The brush weight-average molecular weight and grafting density were 19 kg/mol and 0.7 chains/nm², respectively, as determined by thermogravimetric analysis (TGA, TA Instruments Q600 SDT) at a heating rate of 10 °C/min under argon flow between the temperatures of 25 and 550 °C. The glass transition temperature (T_g) of each polymer was measured by differential scanning calorimetry (DSC, TA Instruments Q2000) between the temperatures of 25 and 150 °C. In all cases, two heating/cooling cycles were performed at a heating/cooling rate of 5 °C/min. The T_{σ} values were obtained from the second heating in order to eliminate any thermal history. Details of the TGA and DSC characterization of PMMA, SAN and PMMA-NPs are given in the Supporting Information. EpoxiCure 2 epoxy hardener and epoxy resin were purchased from Buehler. N-type, <100> oriented silicon wafers (dopant Ph, 10–20 Ω · cm resistivity, 475-575 μ m thickness, single side polished) were purchased from Silicon Quest International. P-type, <100> oriented silicon wafers (dopant B, 0.001–0.005 Ω ·cm resistivity, 500 μ m thickness, single side polished) with a 300 nm wet thermal oxide layer were purchased from University Wafer.

Cloud Point Observations. Phase diagrams for the binary and ternary PNCs were first mapped qualitatively via cloud point observations. This was defined as the temperature at which the film changed from transparent to opaque when viewed against a black background. Polymer solutions with varying compositions were dissolved in methyl isobutyl ketone (MIBK, ≥98.5%, Certified ACS, Fisher Chemical) and stirred for 24 h using a magnetic stir bar. The solutions (17 wt % in MIBK) were spin-coated (1000 rpm, 60 s) onto 1 cm² glass substrates (washed with methanol and toluene and dried under nitrogen flow) and dried at 105 °C for 1 h to remove the residual solvent. All films were smooth and homogeneous as-cast. Film thickness, measured with reflectometry (Filmetrics F3-UV), ranged from 2000 to 2500 nm depending on the composite composition. Samples were subsequently annealed to the desired temperature on a hot stage (Mettler FP-82, Mettler Toledo, Inc.) under continuous argon flow and immediately quenched to room temperature after 24 and 72 h of annealing

Small-Angle X-ray Scattering (SAXS). To prepare samples for small-angle X-ray scattering, PNC solutions (17 wt % in MIBK) were spin-coated (1000 rpm, 60 s) onto 1 cm² silicon wafers with a 300 nm thermal oxide layer and then dried at 105 °C for 1 h to remove the residual solvent. Following drying, the samples were annealed on a hot stage for varying amounts of time under continuous argon flow and then immediately quenched to room temperature. To lift the films, the edges of the substrate were scored and then floated on a 1:5 vol % solution of NaOH (50% w/w NaOH) and deionized water (DI H₂O). After lifting from its substrate, the films were transferred to pure DI H₂O and then onto 2 × 2 cm² Kapton films. In order to achieve a sufficient signal-to-noise ratio, four films were stacked on top of one another, resulting in a film stack thickness of ca. 10 μ m. The films were allowed to dry for 6 h at room temperature between each sequential stack. SAXS measurements were performed on a Xenocs Xeuss 2.0 at the University of Pennsylvania, with a sample-todetector distance of 6.36 m with a Cu K_{α} source, providing an available q-range of 0.003–0.09 Å⁻¹. Raw two-dimensional scattering images were collected on a Pilatus 1 M detector for 20 min per sample and were then azimuthally integrated into one-dimensional patterns for analysis using Foxtrot software.

Transmission Electron Microscopy (TEM). To prepare the samples for electron microscopy characterization, the floated films (see Small-Angle X-ray Scattering (SAXS) section) were lifted from the liquid—air interface of the NaOH solution, transferred onto Teflon, and sputter-coated with a gold and palladium layer (a guide for the eye during microscopy). After sputter-coating, the specimens were lifted from the Teflon and embedded in two-part epoxy. Once the epoxy cured, ca. 70 nm cross sections of the PNCs were prepared by ultramicrotomy (Leica Ultracut S Ultramicrotome) with a room temperature diamond knife. TEM characterization of the ultramicrotomed cross sections, transferred onto carbon-coated TEM grids, was performed with a JEOL JEM-1400 TEM at 120 kV. Radial autocorrelation functions of TEM images were produced to discern the average center-to-center interparticle distances (ID) of the grafted nanoparticles in as-cast films using Gwyddion software.

COMPUTATIONS

Coarse-Grained (CG) Model. Graft and matrix polymers (denoted with subscripts G and M, respectively) were modeled as bead-spring chains with harmonic bonds in CG simulations. The PMMA graft (G) and PMMA matrix chains (matrix_2, M2) were composed of $N_{\rm G}$ and $N_{\rm M2}$ number of CG beads, where each bead of diameter 1d was equal to the Kuhn segment length of PMMA (1.53 nm). The first bead of each graft chain is tethered to the nanoparticle of size $D_{\rm p}$ via a surface grafting site. The number of grafting sites on the nanoparticle was chosen based on the particle size and the desired surface grafting density. The SAN matrix chains (matrix_1, M1) were composed of $N_{\rm M}$ number of CG beads, each bead of diameter 1d as the Kuhn segment of SAN is

similar to that of PMMA. In all chains, the harmonic bonds were modeled using the form

$$U_{\text{bond}}(r) = k_{\text{bond}}(r - r_{\text{o}})^2 \tag{1}$$

with the force constant $k_{\rm bond}$ = 50 kT/ d^2 and the equilibrium bond distance $r_{\rm o}$ = 1d. No angle restrictions were imposed on the graft and matrix CG beads to model flexible graft and matrix chains.

Pairwise non-bonded interactions between all graft and matrix bead pairs (GG, GM1, and M1M1 for binary PNCs and GG, GM1, GM2, M1M1, M1M2, and M2M2 for ternary PNCs) were modeled using the cut and shifted Lennard-Jones²⁸ (LJ) interaction potential given by

$$U_{ij}(r) = \begin{cases} 4\varepsilon_{ij} \left[\left(\frac{\sigma_{ij}}{r} \right)^{12} - \left(\frac{\sigma_{ij}}{r} \right)^{6} \right] + \varepsilon_{ij}; & r \le 2.0\sigma_{ij} \\ 0; & r > 2.0\sigma_{ij} \end{cases}$$
(2)

with $\sigma_{ij} = 1d$ for all pairs. In the case of binary PNCs, $\varepsilon_{ii} = 0.1$ kT for all like beads pairs (GG, M1M1) and $\varepsilon_{\rm GM1}$ is varied from 0.2 to 0.07 kT, thereby tuning the graft-matrix interaction from being energetically favorable ($\varepsilon_{\rm GM1}$ = 0.2 kT), to athermal ($\varepsilon_{\rm GM1}$ = 0.1 kT), and finally unfavorable at $\varepsilon_{\rm GM1}$ = 0.09 kT and 0.07 kT. Thus, the LCST transition for graft (PMMA) and matrix_1 (SAN) polymer chemistries with increasing temperature is captured by decreasing $\varepsilon_{\rm GM1}$ in the model. Accordingly, PNCs with $\varepsilon_{\rm GM1}$ = 0.2 kT correspond to PNCs at low temperatures in experiments (below LCST), while PNCs with $\varepsilon_{\rm GM1}$ = 0.1 kT and $\varepsilon_{\rm GM1}$ = 0.07 kT correspond to PNCs at intermediate and high temperatures in experiments, respectively. In the case of ternary PNCs, the GG and M1M1 bead pairwise interactions were similar to the binary PNCs. With G and M2 beads representing the same chemistry, the ε_{ii} for all G bead pairwise interactions were identical to M2 bead pairwise interactions (i.e., $\varepsilon_{\rm GG} = \varepsilon_{\rm M2M2} =$ 0.1 kT, $\varepsilon_{\rm GG}$ = $\varepsilon_{\rm GM2}$ = 0.1 kT, $\varepsilon_{\rm GM1}$ = $\varepsilon_{\rm M2M1}$). Lastly, all pairwise interactions involving the nanoparticle (with pairs ij = PP, PG, PM1, and PM2) were modeled as purely repulsive using the Weeks–Chandler–Andersen (WCA $\bar{
m J}^{29}$ potential with ε_{ij} = 0.5 kT and σ_{ii} equal to the mean diameter of ij beads pairs.

Parameters Varied. The relative lengths of graft and matrix polymer chains were based on relative molecular weights for PMMA and SAN polymers used in experiments (Table S1). We selected $N_G = 15$ and $N_{M1} = 75$ for both binary and ternary cases. In the case of ternary PNCs, the matrix polymer was composed of two types of polymer matrix chains: $N_{\rm M1}$ = 75 and $N_{\rm M2}$ = 15. The size of the nanoparticle, $D_{\rm P}$ = 5d, and surface grafting density of graft polymer chains, $\Sigma = 0.76$ chains d^2 , were maintained constant for all PNCs. We note that, in the computations, the above choices of particle diameter and graft and matrix chain lengths were smaller than those in experiments but maintained a similar ratio of matrix to graft chain length, particle curvature, and grafted monomer crowding as in the case of experiments (see Table S1). For all cases, the fraction of any volume occupied by particle, graft, and matrix (M1 and/or M2) beads is kept at $\eta = 0.36$; this packing fraction approaches the behavior of an incompressible melt-like polymer matrix. PNC composition was defined in terms of two parameters: the grafted NP filler fraction,

terms of two parameters. The $\phi_{PGP} = \frac{V_{graft} + V_{particle}}{V_{graft} + V_{particle} + V_{matrix_1} + V_{matrix_2}}$, and the matrix_2 volume fraction, $\phi_{M2} = \frac{V_{matrix_1} + V_{matrix_2}}{V_{graft} + V_{particle} + V_{matrix_1} + V_{matrix_2}}$. For binary and

ternary PNCs, the SAN polymer matrix volume fraction is $1 - \phi_{\text{DGP}} - \phi_{\text{M2}} = \phi_{\text{M1}}$.

 $\phi_{\rm PGP} - \phi_{\rm M2} = \phi_{\rm M1}.$ Molecular Dynamics (MD) Simulations. The LAMMPS³⁰ package was leveraged to perform the MD simulations with the CG model for PNCs (vide supra). For all simulations, the starting configuration consisted of a nanoparticle of size $D_P = 5d$ grafted with 60 chains, leading to a grafting density of 0.76 chains d^2 . The grafted chains were relaxed from the starting configuration during a short simulation run with all (GG and PG) interactions set as purely repulsive using the WCA potential. The relaxed grafted nanoparticle configuration was placed in a large box ($\eta \approx$ 0.006), with ϕ_{PGP} = 0.01, along with matrix chains with the desired composition defined by the $\phi_{
m M2}$ value. The large simulation box volume allowed mixing of graft and matrix chains in the NVT ensemble for 5×10^6 time steps, at a reduced temperature of $T^* = 1$ maintained using the Nosé-Hoover^{31,32} thermostat with a damping time of 1 τ . In this mixing stage, the equations of motion were integrated using the velocity Verlet algorithm with time step $\Delta t = 0.001 \tau$. The cubic simulation box was then shrunk isotropically in all three dimensions over 2×10^6 time steps to achieve a final simulation box volume packing fraction of η = 0.36. At the final box size, PNC configurations were further equilibrated for $1 \times$ 10⁷ time steps with $\Delta t = 0.005 \tau$, and equilibrated configurations were then used to generate production run configurations every 10^5 time steps for an additional 2×10^7 time steps to perform structural analyses.

MD simulations of a single grafted nanoparticle in a polymer matrix with a low $\phi_{PGP} = 0.01$ were performed with ϕ_{M2} ranging from 0 (binary case with matrix chain length $N_{\rm M1}$ = 75) to $\phi_{M2} = 0.043$ and 0.1 (ternary cases with a low volume fraction of matrix_2 chains similar to matrix_2 composition used in experiments; see Table S2). An additional case of ϕ_{M2} = 0.99 (\approx 1) corresponding to a binary PNC case with the matrix entirely composed of matrix_2 chains of length $N_{\rm M2}$ = 15 (and $\phi_{\rm M1}$ = 0) was run as well. Additionally, for PNC cases of experimental relevance with higher grafted filler fractions of $\phi_{\text{PGP}} = 0.039, 0.079, \text{ and } 0.205 \text{ and with aforementioned } \phi_{\text{M2}}$ values, polymer reference interaction site model (PRISM) theory calculations described below were performed. This combination of MD simulations and PRISM theory enables calculation of structure factors at large length scales (i.e., at small scattering wave vector (q) values) with a significantly lower computational expense than MD simulations by eliminating the need to run large system sizes of multiparticle PNCs with high ϕ_{PGP} . Furthermore, unlike MD simulations, PRISM theory results are devoid of artifacts arising from chosen simulation box/system sizes and/or kinetic trapping effects.

Polymer Reference Interaction Site Model (PRISM) Theory. Polymer reference interaction site model (PRISM) 33-35 theory is a liquid-state theory that describes structure in polymer solutions and melts using the Ornstein–Zernike 36-like mathematical form

$$\hat{H}(\mathbf{q}) = \hat{\Omega}(\mathbf{q})\hat{C}(\mathbf{q})[\hat{\Omega}(\mathbf{q}) + \hat{H}(\mathbf{q})]$$
(3)

Here, $\hat{H}(\mathbf{q})$ is an $N \times N$ matrix composed of the total intermolecular pair correlations, $\hat{C}(\mathbf{q})$ is an $N \times N$ matrix composed of direct pair correlations, and $\hat{\Omega}(\mathbf{q})$ is an $N \times N$ matrix composed of intramolecular pair correlations. N is the number of interaction site types, which in this study can be three or four types of interaction sites corresponding to

particle, graft, matrix_1, and/or matrix_2 beads depending on the chosen matrix composition ($\phi_{\rm M2}$ = 0, 0.043, 0.1, and 1) for PNCs. Although graft and matrix_2 beads refer to the same chemistry (PMMA), they are designated as separate types of interaction sites since the intramolecular correlations for tethered graft chains are expected to be significantly different from matrix 2 chains.

The intramolecular pair correlation matrix, $\hat{\Omega}(\mathbf{q})$, given as an input to the PRISM theory, is composed of intramolecular structure factor elements, $\widehat{\omega}_{XY}(\mathbf{q})$, for site pairs XY in each molecule. At any PNC grafted filler fraction ($\phi_{PGP}=0.039$, $\phi_{PGP}=0.079$, and $\phi_{PGP}=0.205$) and matrix_2 filler fraction ($\phi_{M2}=0$, 0.043, 0.1, 1), $\widehat{\omega}_{XY}(\mathbf{q})$ was approximated³³ from single-particle PNC MD simulations at low $\phi_{PGP}=0.01$ and low $\phi_{M2}=0.043$ as follows:

$$\widehat{\omega_{XY}}(\mathbf{q}) = \left\langle \frac{1}{N_X + N_Y} \sum_{i=1}^{N_Y} \sum_{j=1}^{N_X} \frac{\sin(\mathbf{q}r_{ij})}{\mathbf{q}r_{ij}} \right\rangle$$
(4)

where N_X and N_Y are the total number of interaction sites of type X and type Y, respectively, within the same molecule, and r_{ij} is the intersite distance.

The PRISM equation is numerically solved for total intermolecular pair correlation, $\hat{H}(\mathbf{q})$ and direct pair correlation matrix, $\hat{C}(\mathbf{q})$. Each element of the $\hat{C}(\mathbf{q})$ matrix is a pairwise direct site correlation function, c_{XY} , expressed using a closure equation, in terms of the interaction potential, U_{XY} , and the total intermolecular pair correlation, h_{XY} , of any site pair XY. For particle—particle pair, hypernetted chain closure $(HNC)^{37,38}$ was used as follows:

$$c_{\rm pp}(r) = h_{\rm pp}(r) - \ln[h_{\rm pp}(r) + 1] - \beta U_{\rm pp}(r), r > D_p$$
(5)

For the remaining site pairs, XY (GG, GM1, GM2, M1M1, M1M2, M2M2, PG, PM1, and PM2), Percus—Yevick (PY)^{33,35,39,40} closure was used as

$$c_{XY}(r) = (1 - e^{\beta U_{XY}(r)})(h_{XY}(r) + 1), \quad r > d_{XY}$$

 $(h_{XY}(r) + 1) = g_{XY}(r) = 0, \qquad r \le d_{XY}$ (6)

with d_{XY} equal to the mean diameter of sites X and Y.

For a given input, the output in the form of pairwise total intermolecular correlations for all pairs of sites, in real and Fourier space was obtained upon numerically solving eqs 3, 5, and 6 using the pyPRISM⁴¹ package.

Analyses. The spatial arrangement of graft, matrix_1, and matrix_2 beads as a function of distance from the particle surface was quantified from configurations sampled in MD simulation trajectories in the form of concentration profiles defined as

$$C_{i|r} = \left\langle \frac{n_i(r)}{4\pi r^2 \Delta r} \right\rangle \tag{7}$$

where i refers to the bead type (G, M1, or M2) and n_i refers to the number of beads of type i within a shell volume of thickness Δr at a distance r from the grafted nanoparticle surface. To plot the graft and matrix concentration profiles, C_{ilr} was normalized with C_{ilr} at r=0 (surface) for graft beads and C_{ilr} at $r=\infty$ (bulk) for matrix_1 and matrix_2 beads. This normalized fraction is denoted as $C_{ilr}/C_{ilr=0}$ and $C_{ilr}/C_{ilr=\infty}$ for graft and matrix beads, respectively.

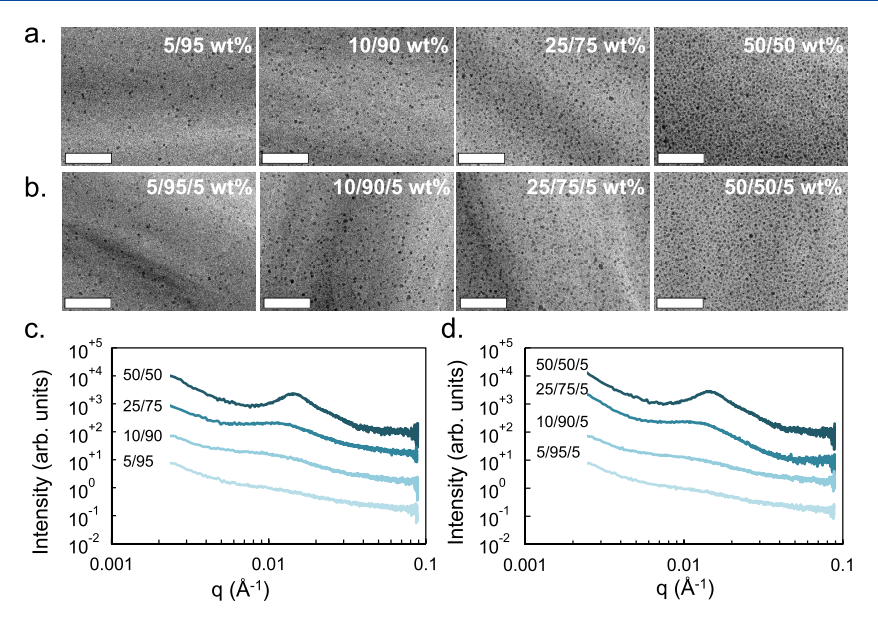


Figure 1. Representative cross-sectional TEM micrographs of ultramicrotomed as-cast (a) binary (PMMA-NP/SAN) and (b) ternary (PMMA-NP/SAN/PMMA) films as a function of nanoparticle loading showing individually dispersed PMMA-NPs. Image scale bars are 300 nm. Panels (c) and (d) show the corresponding 1D SAXS profiles for the binary and ternary PNC films. The profiles are vertically shifted for clarity.

The thickness of the graft polymer layer on the nanoparticle surface was quantified by calculating the ensemble averaged grafted brush height, $H_{\rm b}$, from the MD simulation configurations, defined as

$$H_{\rm b} = \left\langle \sqrt{\frac{\sum_{\rm 1}^{n_{\rm G}} r_{\rm i}^2}{n_{\rm G}}} \right\rangle \tag{8}$$

with r_i equal to the distance of an ith graft polymer bead from the surface of the particle and $n_{\rm G}$ equal to the total number of graft polymer beads on the particle (*i.e.*, $N_{\rm G}$ times the number of graft chains on the particle). All quantities from MD simulations are reported as block averages obtained from four blocks of 50 configurations each, and the error bars are standard deviations in the average values of the four blocks.

The structural output from PRISM theory calculations include the total intermolecular correlation matrix, $\hat{H}(\mathbf{q})$, with the elements of the matrix $h_{XY}(\mathbf{q})$ for a site pair XY converted to real space counterparts, $h_{XY}(r)$. The intermolecular pair correlation function in real space, $g_{XY}(r)$, is calculated from $h_{XY}(r)$ as follows

$$g_{XY}(r) = h_{XY}(r) + 1$$
 (9)

In Fourier space, the structure factor matrix, $\hat{S}(\mathbf{q})$, is obtained using $\hat{H}(\mathbf{q})$ and $\hat{\Omega}(\mathbf{q})$ as

$$\hat{S}(\mathbf{q}) = \hat{H}(\mathbf{q}) + \hat{\Omega}(\mathbf{q}) \tag{10}$$

The elements of the structure factor matrix include the particle–particle structure factor, $S_{PP}(\mathbf{q})$, and graft–graft structure factor, $S_{GG}(\mathbf{q})$.

■ RESULTS AND DISCUSSION

As-Cast Binary and Ternary PNCs. Figures 1a and 1b show representative TEM micrographs of as-cast (*i.e.*, room temperature) binary and ternary PNC films as a function of composition, respectively. The binary PMMA-NP/SAN polymer blend nanocomposites are denoted by A/B, where A and B represent the weight fractions of PMMA-NP and

SAN, respectively. The ternary PMMA-NP/SAN/PMMA PNCs are denoted by A/B/C, where A and B are the weight fractions of PMMA-NP and SAN from the binary PNCs, and C is the weight fraction of the PMMA compatibilizer with respect to the total amount of polymer (PMMA-NP, PMMA, and SAN). This notation is adopted to more easily compare the two systems. 19 The images reveal that the films exhibit remarkable dispersion of particles with little to no clustering. The lowest loadings of particles (5/95 and 5/95/5) result in average center-to-center interparticle distances (ID) of ca. 70 nm, as determined through image analysis using ImageJ. The IDs decrease rapidly as the weight percent of NPs increases, resulting in a value of ca. 30 nm at the highest loadings (50/50 and 50/50/5). Transmission SAXS was utilized as a second method to confirm dispersion and to measure the center-tocenter NP correlation lengths. As shown in Figure 1c,d, a scattering peak occurs at progressively lower q values as the particle loading decreases. The relative magnitude of each peak decreases as the loading decreases, consistent with the reduced scatterer populations (scattering at compositions of 5/95 and 5/95/5 was too weak to produce any discernable peak). IDs extracted from hard sphere structure factor fits to the data were ca. 70 nm ($q \approx 0.009$ Å⁻¹) at 10 wt % NPs and decreases to ca. 42 nm $(q \approx 0.015 \text{ Å}^{-1})$ at 50 wt %. These values are in good agreement with those obtained through autocorrelation functions of each TEM micrograph (Figure S6). For instance, the lowest loadings of particles result in no correlation peak, while the highest loadings (50 wt %) exhibit an average centerto-center ID of ca. 45 nm. For NPs that are randomly distributed in the polymer matrix, the theoretical ID is given

$$ID(\sigma) = d_{\rm m} \left\{ \left(\frac{\pi}{6\varphi_{\rm NP}} \right)^{1/3} \left[\exp(1.5(\ln \sigma)^2) \right] - \exp[0.5(\ln \sigma)^2] \right\}$$

$$(11)$$

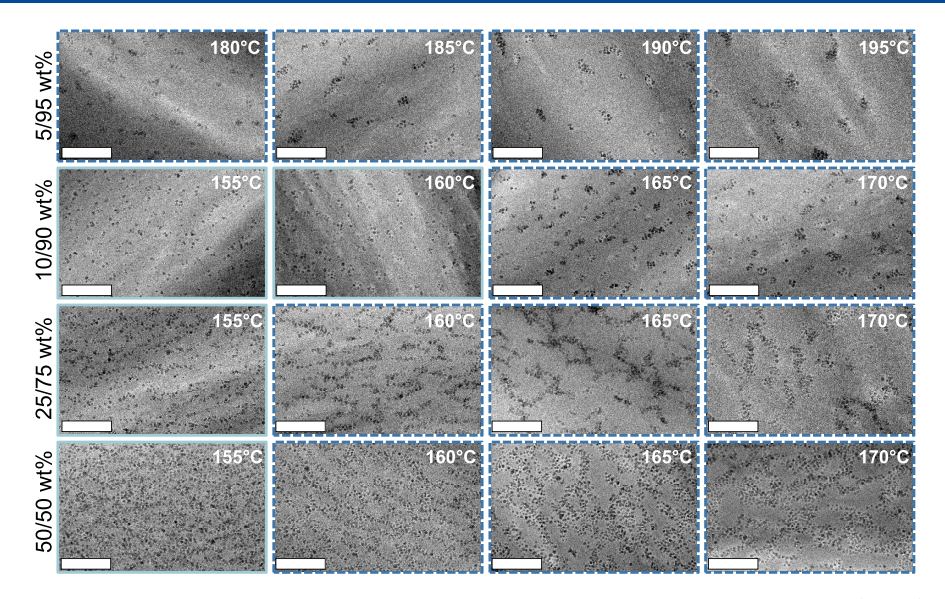


Figure 2. Representative cross-sectional TEM micrographs of ultramicrotomed binary PMMA-NP/SAN = 5/95 (row 1), 10/90 (row 2), 25/75 (row 3), and 50/50 (row 4) films annealed at the indicated temperatures for 24 h. Border colors denote one (teal, solid) and two (blue, dashed) phase regions. The scale bars are 300 nm.

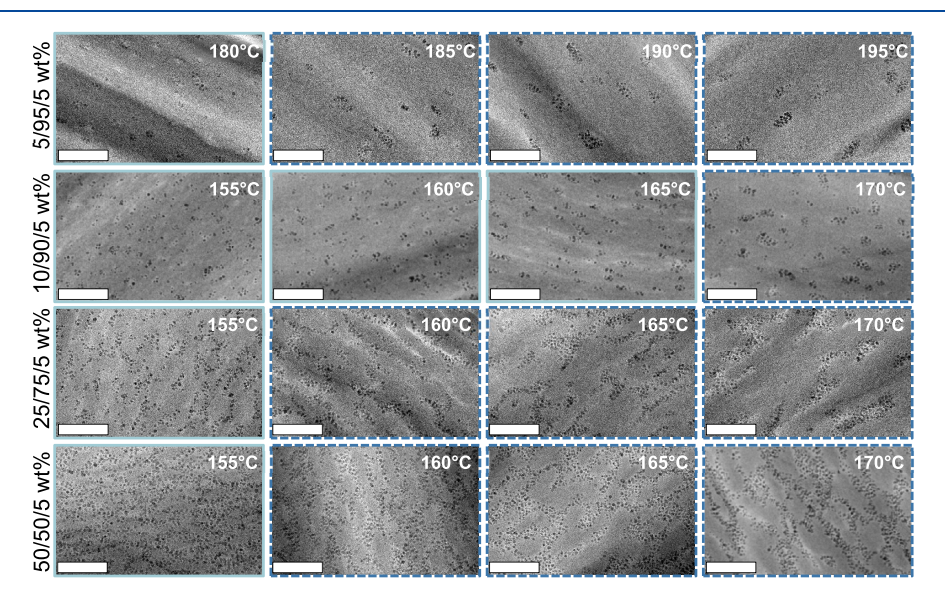


Figure 3. Representative cross-sectional TEM micrographs of ultramicrotomed ternary PMMA-NP/SAN/PMMA = 5/95/5 (row 1), 10/90/5 (row 2), 25/75/5 (row 3), and 50/50/5 (row 4) films annealed at the indicated temperatures for 24 h. Border colors denote one (teal, solid) and two (blue, dashed) phase regions. The scale bars are 300 nm.

where $d_{\rm m}$ is the mean diameter (15.5 nm), $\varphi_{\rm NP}$ is the volume fraction of NP cores, and σ is the NP polydispersity (Equation S2). The ID measured here is consistent with the theoretical predictions, indicating that the as-cast PNC films are homogeneous and mixing between the grafted NP and matrix polymers is thermodynamically favorable (Figure S7).

Phase Separation in Binary and Ternary PNCs. To probe differences in mixing/demixing behavior of the binary and ternary PNC, phase diagrams are mapped out as a function of temperature and composition. Starting with the well-dispersed NP systems at room temperature, the films are annealed between 155 and 195 $^{\circ}$ C and analyzed using a combination of cloud point observations, TEM, and SAXS. The phase diagram of the binary PNC serves as a reference system and is determined by monitoring the cloud point transitions of *ca.* 2 μ m bulk films (Figure S8). The films

transitioned from transparent to opaque with increasing annealing temperature, with a lower critical solution temperature (LCST) of $\approx 160~^{\circ}$ C, consistent with PMMA/SAN blends studied by Newby et al. ⁴⁴ This behavior demonstrates that PMMA grafted nanoparticles ($\Sigma = 0.7~{\rm grafts/nm^2}$) in a SAN matrix exhibit enthalpic interactions comparable to the PMMA/SAN blend. Specifically, the large grafting density of PMMA chains shields the NP core such that core—core interactions are effectively screened. The PNC morphology is therefore dictated by the thermodynamic behavior of PMMA and SAN rather than NPs' core—core interactions. While this binary PNC behavior is not new, ^{12,13} the effect of adding a third component on phase separation is still unknown. Here, we add the identical polymer as the brush, namely, PMMA, at a fixed composition (5 wt %), and match their molecular weights ($M_{\rm w, PMMA} = M_{\rm w, PMMA-NP}$). We can then make direct

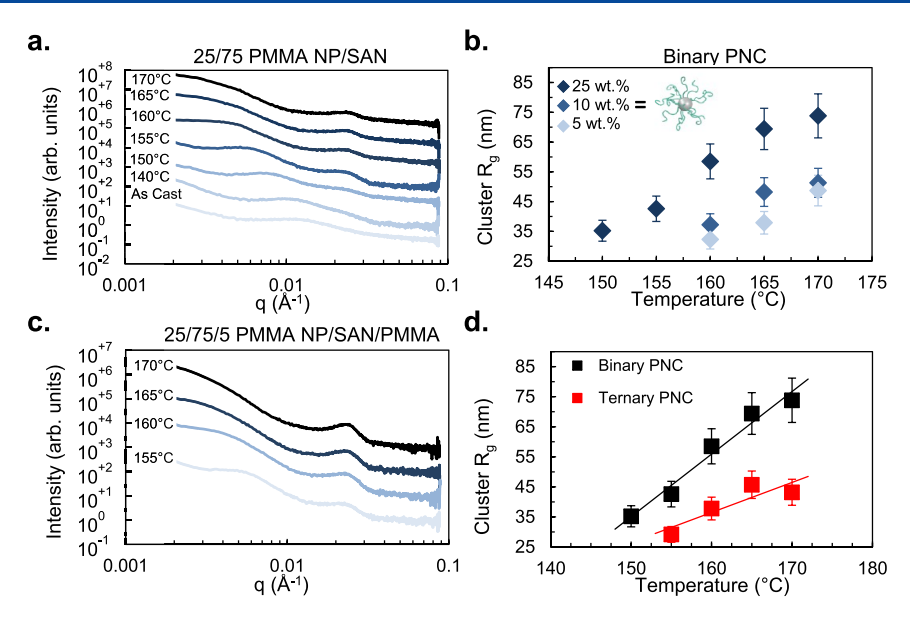


Figure 4. (a) 1D SAXS profiles of 25/75 wt % binary PMMA-NP/SAN films annealed at the indicated temperatures for 24 h. (b) Corresponding average nanoparticle cluster radius of gyration as a function of temperature obtained through SAXS modeling. (c) 1D SAXS profiles for the 25/75/5 wt % ternary PNC under identical annealing conditions to those in (a). A direct comparison of the average aggregate size as a function of temperature for (a) and (c) is shown in (d). The 1D SAXS profiles are vertically shifted to avoid overlap and more clearly track evolutions in scattering peaks.

comparisons between the interactions of SAN matrix and grafted PMMA versus free PMMA chains. Similar to the binary PNC, cloud point measurements (not shown here) were performed on the ternary PNC to determine the phase diagram. Interestingly, cloud point observations suggest a slight increase in miscibility for compositions of 5/95/5 and 10/90/5 where PMMA-NPs are the minority component.

A more quantitative characterization of PNC phase evolution can be obtained from TEM and SAXS. Figure 2 depicts representative TEM images of binary PNCs at varying compositions: PMMA-NP/SAN = 5/95, 10/90, 25/75, and 50/50 after 24 h of annealing at the respective temperatures. At temperatures below the optically determined phase boundary of ≈160 °C, the TEM micrographs reveal that the overall distribution of NPs is homogeneous as shown by the morphologies outlined by the teal solid boxes. Notably, there are several dispersed NP clusters within the one-phase region. This suggests that the potential of mean force between two particles is not purely repulsive and slight aggregation occurs at $T > T_g$, similar to what has been seen previously. ^{45,46} However, as the samples are quenched into the two-phase region, macrophase separation readily occurs as shown by morphologies outlined by the blue dashed boxes. The degree of phase separation appears to increase with temperature, which is expected based on the increased mobility of the constituents and deeper quench depth. Interestingly, discrete NP domains are formed for 5/95 and 10/90 off-critical compositions, whereas the 25/75 system qualitatively exhibits string-like and more connected domains. The 50/50 system exhibits a bicontinuous morphology, similar to the previously reported PMMA/SAN blend. 44,47 Within domains of NP aggregates, the average center-to-center ID is ca. 28 nm as quantified through image analysis. 50/50 samples were also annealed for 72 h in order to confirm that the 24 h annealing times were sufficiently long to reach quasi-equilibrium morphologies (Figure S9). Specifically, after annealing in the one-phase region, no discernable difference in PNC morphologies is observed at

24 and 72 h. Likewise, when annealed in the two-phase region, the aggregate domain size only slightly increases after 72 h compared to 24 h. This comparison indicates that 24 h is sufficient to distinguish between one-phase and two-phase morphologies in the binary and ternary PNCs.

Figure 3 shows cross-sectional TEM micrographs for ternary compositions analogous to the binary systems shown in Figure 2 after 24 h of annealing at the indicated temperatures. For 5/ 95/5 films, particles remain dispersed at temperatures up to 180 °C. At temperatures of 185 °C and higher, the uniform distribution of NPs becomes disrupted and the NPs form discrete aggregates that increase in size as the temperature increases. Similarly, 10/90/5 films exhibit macrophase separation into discrete domains at a temperature of 170 °C. While comparable, the reduced domain size for the 10/90/5 composite compared to the 5/95/5 is attributed to the smaller thermodynamic driving force and slower diffusivity at lower temperatures. The phase separation evolution of PNCs near the phase separation temperature (≈160 °C) and at intermediate compositions (i.e., 25/75/5 and 50/50/5) shows a transition from dispersed to aggregated, forming string-like and bicontinuous morphologies, respectively.

While these trends for ternary composites are similar to the binary composite, several interesting features emerge. Specially, off-critical compositions of 5/95/5 (180 °C) and 10/90/5 (165 °C) reveal, on average, uniformly distributed particles and clusters of a much smaller size compared to their binary counterpart. At 180 °C, 5/95/5 ternary composites exhibit significantly less aggregation compared to the binary analogue (Figure \$10). This aggregation suppression is also observed in the 10/90/5 case but less pronounced. Compositions approaching the critical composition show no appreciable difference in miscibility upon addition of linear PMMA, similar to what was observed in the cloud point transitions.

We performed SAXS measurements on the annealed PNCs in parallel with TEM to further quantify the length scales of phase separation as a function of temperature and NP loading.

Figure 4a shows the 1D scattering intensity as a function of wave vector for a representative 25/75 wt % binary PNC (data for other compositions are in the Supporting Information). The background-subtracted one-dimensional scattering intensities were modeled using two scattering contributions to represent isolated/paired NPs and aggregated NP clusters (see the Supporting Information). We first consider the scattering profile for the as-cast samples, which shows a single, weak scattering feature near $q \approx 0.0123 \text{ Å}^{-1}$. This represents the average center-to-center interparticle distance (51 nm), which is greater than the diameter of a single grafted NP. This observation is consistent with well-dispersed NP cores, in agreement with TEM images in Figure 1. However, after annealing, we observe the emergence of two separate scattering features: one at a higher q and one at a lower q. The peak position of the higher q feature remains relatively unchanged at higher temperatures, while the lower q feature increases in intensity while also moving to even smaller values. Modeling of the data indicates that the higher q feature represents the average center-to-center interparticle distance, which initially (slightly) decreases with increasing temperature and eventually becomes well-defined as the PMMA-NPs aggregate at elevated temperatures. The lower q feature represents the scattering between the small nanoparticle clusters as seen in Figures 2 and 3, which continue to grow at elevated temperatures as smaller clusters coalesce. Both of these observations indicate a phase transition between ≈150 and 160 °C, commensurate with observations from TEM. The scattering feature representing the aggregated NPs can be used to determine the average size of a single "cluster" of NPs. For the binary composite at 5, 10, and 25 wt %, Figure 4b shows how the average cluster radius of gyration (R_g) increases as the temperature increases, consistent with an increase in the thermodynamic driving force for phase separation. For example, at 25 wt %, Rg increases by more than a factor of two as the temperature increases from 150 to 170 °C. There is also a significant increase in the cluster size as the NP loading increases from 10 to 25 wt %, consistent with a smaller as-cast interparticle distance at higher loading (cf. Figure S7). Namely, because NPs are initially closer to one another at higher loadings, larger aggregates are easier to form for the same annealing times.

It is important to note that, even at temperatures below the LCST (160 °C), a shoulder can be observed in the scattering intensity (Figure 4a) at q values close to the aggregate ID. Based on the TEM micrographs in Figure 2, we interpret this as the formation of small NP clusters when LCST > T > $T_{\rm g}$ even though macrophase separation is not thermodynamically favorable. Annealing the samples above their glass transition allows the NPs to diffuse more readily, leading to the formation of small clusters due to the short-range attractive forces between the particles noted earlier. Noticeably, the measured ID (28 nm) for the center-to-center interparticle distance is slightly less than the diameter of the PMMA-NP, suggesting that PMMA brushes are weakly interpenetrating with one another at elevated temperatures.

Figure 4c shows scattering data for the PMMA-NP/SAN/PMMA ternary composite at identical NP loadings as the binary system shown in Figure 4a. Modeling of the data reveals two notable differences between the binary and ternary systems. First, the high-q scattering feature is at slightly smaller q values in the ternary PNC than in the binary one at 170 °C (0.024 Å⁻¹ vs 0.026 Å⁻¹, respectively). This is

attributed to less PMMA brush interdigitation and a lower degree of brush collapse, indicative of a slightly more miscible PNC. Second, the average NP aggregate size is smaller in the ternary composite than in the binary case. This reduction in cluster size is substantially more than what one could surmise from a simple dilution argument through the addition of the ternary component. Figure 4d compares the aggregate size as a function of temperature for the binary (black squares) and ternary (red squares) systems. Here, it is worth noting that, in addition to smaller aggregate sizes, the difference between aggregate sizes of the binary and ternary PNCs increases as the temperature increases. The addition of only 5 wt % PMMA homopolymer decreases the average aggregate size by as much as a factor of two at 170 °C, indicating a suppression in aggregation and an increase in PNC miscibility.

Figure 5 shows a phase diagram for both binary and ternary composites constructed by compiling cloud point, TEM, and

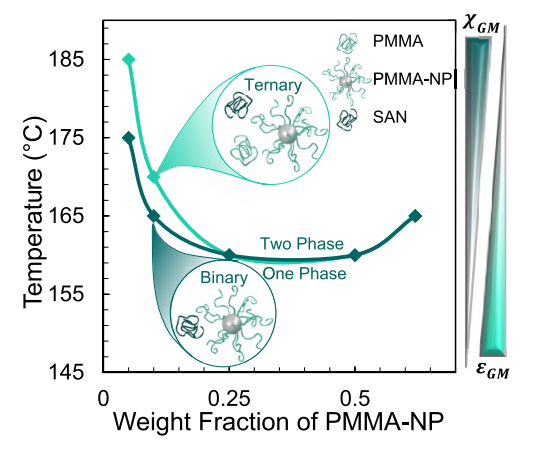


Figure 5. Phase diagrams of binary PMMA-NP/SAN and ternary PMMA-NP/SAN/PMMA nanocomposites. The ternary composites exhibit increased miscibility in off-critical compositions. The solid lines have been drawn to guide the eye.

SAXS results. Near the critical temperature, the binary phase diagram is relatively flat between 20 and 50 wt % PMMA-NP and increases sharply below 10 wt % and above 63 wt %. Accounting for the polydispersity of SAN, this behavior is consistent with other blends containing a polydisperse component.⁴⁸ From the observed phase separation behavior, the addition of linear PMMA increases the miscibility of the binary PMMA-NP/SAN system at the most off-critical compositions (i.e., 5/95/5) by as much as 10 °C. To begin to understand this, we recall the work presented by Schmitt et al., who studied a binary system of silica particles grafted with polystyrene (PS) and PMMA ligands with an upper critical solution temperature (UCST). 12 They demonstrated that the specific ligand interactions in mixtures of these polymer-grafted nanoparticles impart a similar phase behavior as in analogous linear polymer blends, similar to our findings for PMMA/SAN systems. 12 While general trends in phase behavior between the two systems were alike, distinct differences were recognized. Specifically, the binary PNC demonstrated increased miscibility and slower kinetics of domain growth as compared to the neat polymer blend. The apparent increase in miscibility was rationalized as a consequence of a reduced thermodynamic driving force for phase separation attributed to fewer unfavorable segmental interactions between PMMA-PS ligands. Additionally, the presence of NP cores resulted in a

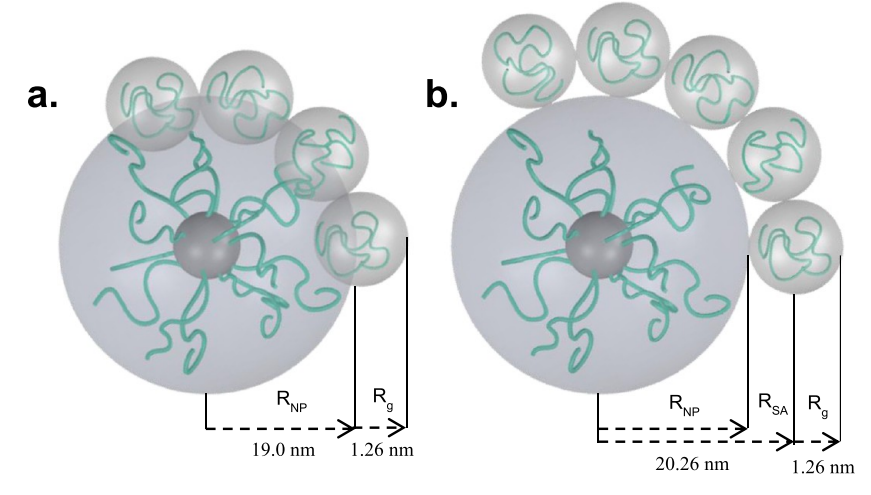


Figure 6. This cartoon illustrates two possible scenarios of linear PMMA covering the surface of the PMMA-NPs. Case one (a) assumes that linear PMMA chains wet the PMMA-NP brush layer. Case two (b) adopts both PMMA-NPs and linear PMMA as hard spheres, resulting in complete exclusion of PMMA chains within the brush corona.

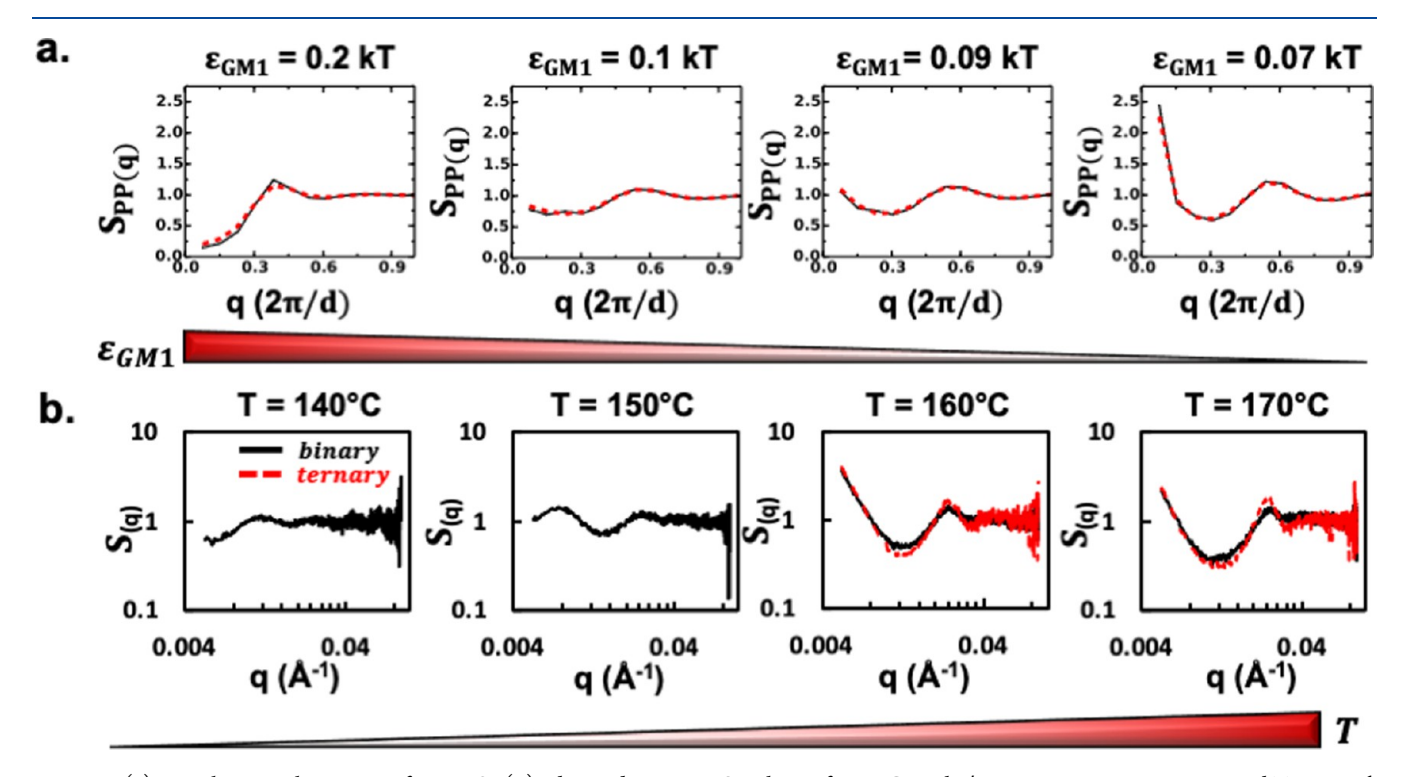


Figure 7. (a) Particle–particle structure factors, $S_{PP}(\mathbf{q})$, obtained using PRISM theory for PNCs with $\phi_{PGP}=0.205$, $\varepsilon_{GG}=\varepsilon_{M1M1}=0.1$ kT, $D_P=5d$, $N_G=15$, $N_{M1}=75$, $N_{M2}=15$, and $\Sigma=0.76$ chains/ d^2 and (left to right) $\varepsilon_{GM1}=0.2$ kT, $\varepsilon_{GM1}=0.1$ kT, $\varepsilon_{GM1}=0.09$ kT, and $\varepsilon_{GM1}=0.07$ kT. The binary PNC case with $\phi_{M2}=0$ is shown as a black line, and the ternary case with $\phi_{M2}=0.043$ (5 wt %) is shown as a red dashed line. (b) Corresponding particle–particle structure factors, $S(\mathbf{q})$, obtained using SAXS for 25/75 wt % PNCs.

smaller number density of segmental contacts. ¹² Here, it is important to reiterate that these segmental interactions are unfavorable due to the systems UCST behavior. Therefore, the UCST work by Schmitt and co-workers is consistent with the presented LCST work thus far, with our results demonstrating that the addition of linear PMMA reduces aggregation of PMMA-NPs and increases miscibility. We attribute this phenomenon to an interfacial compatibilization between the SAN matrix and grafted PMMA brush due to localization of the free PMMA chains. The addition of linear PMMA increases the number of favorable segmental contacts between each chemical species and therefore reduces the thermody-

namic driving force for phase separation (parsing of the specific enthalpic and entropic contributions to this will be discussed later). Importantly, this miscibility increase was only observed for 5/95/5 and 10/90/5 off-critical compositions. These experimental observations will be supported by PRISM calculations and MD simulations (vide infra).

The improved miscibility from homopolymer compatibilization can be understood from a simple geometric model that considers the interaction between the free and grafted PMMA chains. Under the assumption that the free PMMA chains are Gaussian coils with a pervaded volume described as spheres, the number of chains needed to cover the surface area of a

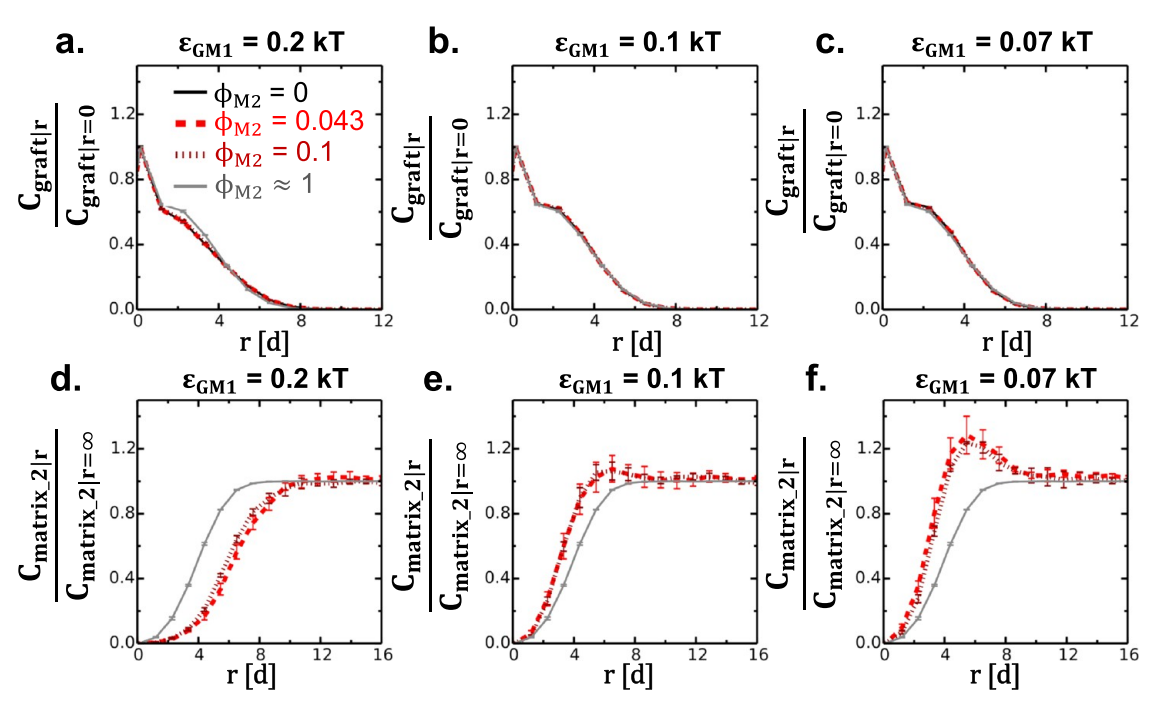


Figure 8. Concentration profiles for graft, G (a-c) and matrix_2, M2 (d-f) beads as a function of distance from the particle surface, r [in units of d] using MD simulations for PNCs with $\varepsilon_{\rm GM1}$ = 0.2 kT (a, d), $\varepsilon_{\rm GM1}$ = 0.1 kT (b, e), and $\varepsilon_{\rm GM1}$ = 0.07 kT (c, f). Colored lines represent varying volume fractions of matrix_2 chains with $\phi_{\rm M2}$ = 0 (black line), $\phi_{\rm M2}$ = 0.043 (red dashed line), $\phi_{\rm M2}$ = 0.1 (dark red dotted line), and $\phi_{\rm M2}$ \approx 1 (gray line). The legend in part (a) applies to all parts in this figure. These results are for $\varepsilon_{\rm GG} = \varepsilon_{\rm M1M1} = 0.1$ kT, $D_{\rm P} = 5d$, $N_{\rm G} = 15$, $N_{\rm M1} = 75$, $N_{\rm M2} = 15$, Σ = 0.76 chains/ d^2 , and $\phi_{\rm PGP}$ = 0.01. The error bars have been obtained from block averages of four blocks of 50 configurations each, sampled in a simulation run.

PMMA-NP can be directly calculated. 49 As shown in Figure 6, two regimes are considered: (1) PMMA chains wetting the PMMA brush (wet brush state) and (2) PMMA excluded from the PMMA brush layer (dry brush state). For the wet brush case, ca. 650 homopolymer chains are needed to completely cover a PMMA-NP/matrix interface, whereas ca. 740 chains are needed for the dry brush state. The total number of available PMMA homopolymer chains for compatibilization at a constant 5 wt % loading can be calculated. Under wet brush conditions, the ratio of required to available PMMA chains for the 5/95/5 composite is approximately 1:1. As the composition of the films increases to higher loadings of PMMA-NPs, the ratio decreases to 2:1, 4.5:1, and 9:1 for 10/ 90/5, 25/75/5, and 50/50/5 films, respectively. While similar, the ratios derived for the dry brush regime are smaller given that more PMMA homopolymer is needed to shield the NP surface. Due to the small amount of PMMA-NPs in 5/95/5 films, the proposed scaling model suggests that a 5 wt % addition of PMMA is sufficient to compatibilize the PMMA-NP/SAN system. Specifically, at low loadings of PMMA-NPs, there is sufficient PMMA homopolymer to completely wet the PMMA brush layer, and the resultant phase behavior is dictated by the PMMA homopolymer and SAN interactions. However, as the concentration of NPs increases, 5 wt % PMMA becomes insufficient to completely shield the PMMA brush from the SAN matrix, and the phase behavior is dictated by the brush/matrix interactions as demonstrated by the aforementioned ratios. This behavior is captured by our experimental findings shown in Figure 5 where the highest miscibility increase occurred in 5/95/5 films and progressively decreased with particle loading.

Comparing Computations and Experiments. The compatibilization effect of the added PMMA chains in the

ternary PNCs can be systematically investigated using molecular dynamics simulations and polymer reference interaction site model (PRISM) theory serving as computational comparison to the experimental results. As a reminder, in the model, the notation graft (G) and matrix 2 (M2) refer to grafted PMMA and free PMMA matrix chains, and matrix 1 (M1) refers to the SAN matrix chains in experiments. The choice of the graft-matrix_1 ($\varepsilon_{
m GM1}$), graft-graft ($\varepsilon_{
m GG}$), and matrix_1-matrix_1 ($\varepsilon_{
m M1M1}$) attraction strengths at a constant $\varepsilon_{\rm GG}$ and $\varepsilon_{\rm M1M1}$ of 0.1 kT in our model dictates whether the modeled PNC exhibits net favorable interactions (i.e., below the LCST), effectively athermal interactions, or net unfavorable interactions (i.e., above the LCST). Figure 7a shows a series of particle-particle structure factors calculated using PRISM theory for PNCs with decreasing values of $\varepsilon_{\rm GM1}$; the corresponding structure factors from experiments at increasing temperatures are also shown in Figure 7b. The $S_{pp}(\mathbf{q} \to 0)$ for binary (black solid lines) and ternary (red dashed lines) composites at $\varepsilon_{\rm GM1}$ = 0.2 kT, corresponding to low temperatures in experiments, shows no upturn, suggesting the absence of macrophase separation and confirming that the nanoparticles remain relatively well dispersed. This is in agreement with the experimentally obtained structure factors for systems below the LCST (Figure 7b). For the binary and ternary composites at $\varepsilon_{\rm GM1}$ = 0.1 kT, there is a distinct increase in both the value of $S_{PP}(\mathbf{q} \to 0)$ as well as the slope of $S_{PP}(\mathbf{q})$ at low q values as compared to the PNCs with $\varepsilon_{\rm GM1}$ = 0.2 kT. Furthermore, both PNCs with $\varepsilon_{\rm GM1}$ = 0.09 kT and 0.07 kT show an upturn when $S_{PP}(\mathbf{q} \to 0)$, which is consistent with the shapes of the structure factors obtained from experiments performed at higher temperatures where phase separation occurs. These results confirm that decreasing values of ε_{GM1} at constant $\varepsilon_{\rm GG}$ and $\varepsilon_{
m M1M1}$ in the CG model qualitatively captures

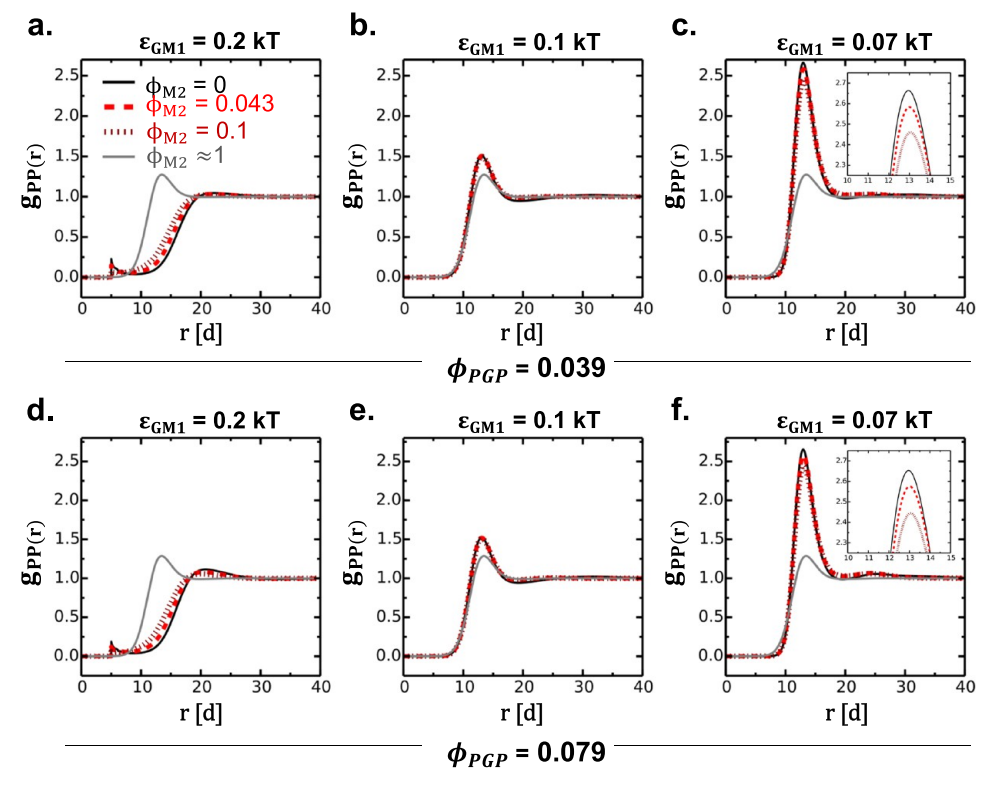


Figure 9. Particle–particle pair correlation function, $g_{PP}(r)$, obtained using PRISM theory for PNCs with $\phi_{PGP} = 0.039$ (a–c) and $\phi_{PGP} = 0.079$ (d–f) with $\varepsilon_{GM1} = 0.2$ kT (a, d), $\varepsilon_{GM1} = 0.1$ kT (b, e), and $\varepsilon_{GM1} = 0.07$ kT (c, f). Varying matrix_2 volume fractions are shown using colored lines with $\phi_{M2} = 0$ (black line), $\phi_{M2} = 0.043$ (red dashed line), $\phi_{M2} = 0.1$ (dark red dotted line), and $\overline{\phi}_{M2} \approx 1$ (gray line). The legend in part (a) applies to all parts in this figure, and the insets in part (c) and part (f) have the same axes labels as the main plots. These results are for $\varepsilon_{GG} = \varepsilon_{M1M1} = 0.1$ kT, $D_P = 5d$, $N_{GI} = 15$, $N_{M1} = 75$, $N_{M2} = 15$, and $\Sigma = 0.76$ chains/ d^2 .

the behavior in experiments with increasing temperature. This CG model can thus be used in MD simulations and PRISM theory to probe and explain the hypothesized compatibilization observed experimentally in the ternary PNCs. Whereas the amount of PMMA in ternary PNCs is kept at 5 wt % for the experimental systems, MD simulations and PRISM theory allow us to systematically investigate the effect of increasing the PMMA matrix volume fraction, ϕ_{M2} , on the structure of the grafted chains and the bulk PNC morphology. In both theory and simulations, the PMMA matrix volume fractions of ϕ_{M2} = 0 and $\phi_{\rm M2}$ = 0.043 correspond to the binary and ternary (5 wt % PMMA) PNC cases in experiments, respectively. Additionally, we also show here the results for a higher ϕ_{M2} case of 0.1 and the limiting case of $\phi_{\rm M2} \approx 1$ (binary PNC with PMMA grafts and chain length matched PMMA matrix) to elucidate the effect of increasing PMMA volume fraction on structure. In the Supporting Information, we present the results for ternary PNCs for all $\phi_{\rm M2}$ ranging from 0 to 1.

First, we use MD simulations to see if we observe compatibilization by quantifying the grafted layer structure and the extent of interpenetration of the matrix_1 and matrix_2 chains into the grafted layer. In binary PNCs (with $\phi_{\rm M2}=0$) when $\varepsilon_{\rm GM1}=0.2$ kT, the net interactions between the graft and matrix_1 (SAN) chains are favorable. However, the matrix_1 chain length is much greater than the graft chain length (i.e., $N_{\rm M1}=75>N_{\rm G}=15$), which leads to entropic driving forces disfavoring graft—matrix_1 interpenetration due to a large loss in conformational entropy of long matrix chains upon wetting the grafted layer. In ternary PNCs with graft and matrix_2 chains being chemically identical and equal in lengths (i.e., $N_{\rm M2}=N_{\rm G}=15$), the shorter matrix_2 (PMMA) chains

have a higher entropic driving force to wet the grafted layer than the enthalpically favored longer matrix_1 (SAN) chains. Thus, it is non-intuitive as to which of these two competing factors dominate. Using concentration profiles of the graft, matrix_1, and matrix_2 chains calculated in MD simulations, we can understand how these two competing forces dictate compatibilization at different $\varepsilon_{\rm GM1}$ values.

Figure 8 shows normalized concentration profiles of the graft (PMMA) and matrix 2 (PMMA) polymers as a function of radial distance from the NP surface for decreasing values of $arepsilon_{
m GM1.}$ At the highest $arepsilon_{
m GM1}$ value (low temperatures) (Figure 8a), the concentration of graft chains in both binary and ternary PNCs with $\phi_{\rm M2} \leq 0.1$ are similar. This suggests that adding low amounts of PMMA (matrix 2) does not alter the spatial arrangement of graft polymers around the particle when $\varepsilon_{\rm GM1}$ is high and $\phi_{\rm M2}$ is low. However, when $\phi_{\rm M2}$ = 1, the concentration of graft polymer at $r \approx 1d-4d$ is slightly higher than in PNCs with $\phi_{\rm M2}$ = 0–0.1. Furthermore, at this high $\varepsilon_{\rm GM1}$ value (low temperatures), the brush height at $\phi_{\rm M2}$ = 1 is smaller than that at lower values of $\phi_{
m M2}$ (Figure S12a). This is because, at a low ϕ_{M2} , the enthalpic driving forces between the SAN matrix and PMMA graft in PNCs extend the graft polymer more than the favorable entropic driving forces in PNCs with shorter PMMA matrix chains at $\phi_{\rm M2} \approx 1$. As $\phi_{\rm M2}$ increases, we do not see a significant difference in matrix 1 bead concentration profiles (Figure S13). The concentration profiles of matrix_2 beads (Figure 8d) show that increasing $\phi_{\rm M2}$ from values of 0.043 to the limiting case of $\phi_{\rm M2} \approx 1$ (gray line) leads to increased penetration of the matrix_2 chains into the grafted layer. This is because at $\varepsilon_{\rm GM1}$ = 0.2 kT and at low $\phi_{
m M2}$ values, the favorable interactions between SAN polymer

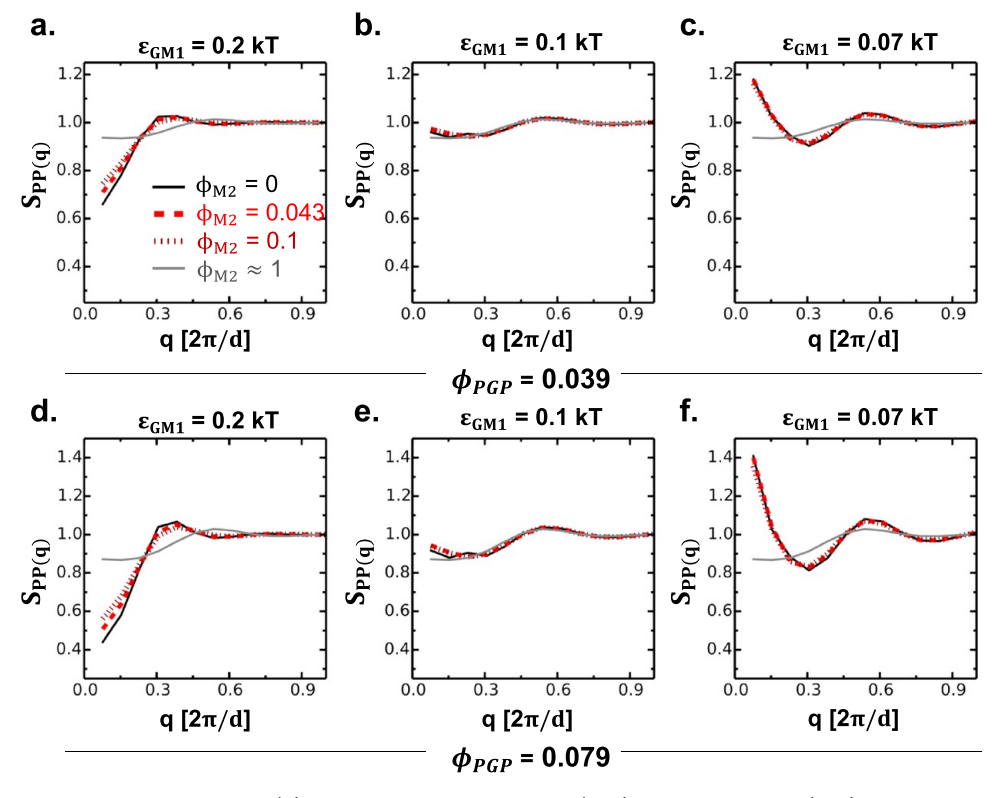


Figure 10. Particle–particle structure factor, $S_{PP}(\mathbf{q})$ for PNCs with $\phi_{PGP} = 0.039$ (a–c) and $\phi_{PGP} = 0.079$ (d–f) with $\varepsilon_{GM1} = 0.2$ kT (a, d), $\varepsilon_{GM1} = 0.1$ kT (b, e), and $\varepsilon_{GM1} = 0.07$ kT (c and f). Varying matrix_2 volume fractions are shown using colored lines with $\phi_{M2} = 0$ (black line), $\phi_{M2} = 0.043$ (red dashed line), $\phi_{M2} = 0.1$ (dark red dotted line), and $\phi_{M2} \approx 1$ (gray line). The legend in part (a) applies to all parts in this figure. These results are for $\varepsilon_{GG} = \varepsilon_{M1M1} = 0.1$ kT, $D_P = 5d$, $N_G = 15$, $N_{M1} = 75$, $N_{M2} = 15$, and $\Sigma = 0.76$ chains/ d^2 .

(matrix_1) and PMMA grafts (graft) compete with the entropically driven penetration of short PMMA matrix chains (matrix_2) to wet the grafted layer. Simulations of PNCs with additional $\phi_{\rm M2}$ values between 0 and 1 (Figure S14d) show that the penetration of matrix_2 chains into the grafted layer progressively increases with an increase in $\phi_{\rm M2}$ at this $\varepsilon_{\rm GM1}$ value.

As $\varepsilon_{\rm GM1}$ decreases to $\varepsilon_{\rm GM1}$ = 0.1 kT (Figure 8b,e), both the graft-matrix_1 and graft-matrix_2 interactions become comparable, and the entropic driving forces cause matrix 2 chains to penetrate the grafted layer more than the long matrix 1 (SAN) chains. 50 Comparison of the matrix 2 concentration profiles in ternary PNCs confirms this higher interpenetration at low values of $\varepsilon_{\rm GM1}$. In Figure 8e, the matrix 2 chain concentration at the end of the grafted layer is slightly greater than that of the bulk. In addition, the concentration of the matrix_2 chain is greater than the binary PNC case when $\phi_{\rm M2} \approx 1$. This suggests that the free PMMA chains are localizing at the PMMA-NP/SAN interface within the ternary PNCs. This effect is further amplified at $\varepsilon_{\rm GM1}$ = 0.07 kT (Figure 8f) where the shorter and athermal matrix_2 chains have a higher concentration near the grafted layer surface because matrix 1 (SAN) chains are not only longer than graft chains (making it entropically unfavorable to interpenetrate the graft layer) but also interact unfavorably with graft chains. The presence of this increased concentration of matrix_2 near the grafted layer only at low values of ε_{GM1} (high temperatures in experiments) agrees with increasing compatibilization seen in experiments (see Figure 4d). Furthermore, Figure 8f and Figure S14f show that this compatibilization effect in ternary PNCs is better at $\phi_{\rm M2}$ =

0.043–0.2 than at $\phi_{\rm M2}$ = 0.4–0.8, based on the higher values of normalized matrix_2 concentration at the edge of the grafted layer for ternary PNCs with $\phi_{\rm M2}$ = 0.043–0.2 than at $\phi_{\rm M2}$ = 0.4–0.8; this suggests an optimal concentration of matrix_2 chains for better compatibilization.

Going beyond the MD simulation results of the graft/matrix interface at a low ϕ_{PGP} , PRISM theory calculations show the impact of varying the grafted nanoparticle and PMMA compatibilizer loadings (ϕ_{PGP} and ϕ_{M2}) on the PNC morphology. The chosen ϕ_{PGP} cases of 0.039 and 0.079 correspond to PNCs with 5/95 and 10/90 PMMA-NP/SAN wt % in experiments (see Table S2), respectively. Figure 9 shows a series of particle—particle pair correlation functions, $g_{PP}(r)$, as a function of ϕ_{M2} and ϕ_{PGP} .

At $\varepsilon_{\rm GM1}=0.2$ kT (Figure 9a), as $\phi_{\rm M2}$ increases, the $g_{\rm PP}(r)$ shifts to lower particle separation distances and exhibits a peak. This is because, as $\phi_{\rm M2}$ increases, the volume fraction of matrix_1 chains that interact favorably with graft chains decreases, resulting in a slight decrease in the brush layer thickness (seen in brush height values plotted in Figure S12) and smaller interparticle distances. This is also confirmed by corresponding $g_{\rm PP}(r)$ plots at intermediate $\phi_{\rm M2}$ values between 0 and 1 shown in Figure S15a.

At $\varepsilon_{\rm GMI}=0.1$ kT (Figure 9b), when the energetic interactions between both graft and matrix_1 and graft and matrix_2 are the same, the $g_{\rm PP}(r)$ peak heights are larger than at $\varepsilon_{\rm GMI}=0.2$ kT, indicating reduced particle dispersion. At this $\varepsilon_{\rm GMI}$, $g_{\rm PP}(r)$ profiles are also similar in PNCs with $\phi_{\rm M2}\leq0.1$, where the majority of the matrix is made of the longer matrix_1 chains. There is no difference between the $g_{\rm PP}(r)$ profiles for the binary PNC ($\phi_{\rm M2}=0$) and ternary PNC with a

low $\phi_{\rm M2}$. Figure S15b shows that the $g_{\rm PP}(r)$ peak height gradually decreases with increasing $\phi_{\rm M2}$ values since the volume fraction of the longer matrix_1 chain is reduced relative to shorter matrix 2 chains in the PNC.

At $\varepsilon_{\rm GM1}=0.07$ kT (Figure 9c), the shapes of the $g_{\rm PP}(r)$ exhibit stronger particle aggregation than at a higher $\varepsilon_{\rm GM1}$ and the $g_{\rm PP}(r)$ peak heights for the ternary PNCs with $\phi_{\rm M2}=0.043$ and 0.1 are slightly smaller (see Figure 9c, inset) than the binary case with $\phi_{\rm M2}=0$. This indicates reduced aggregation of the particles in the ternary PNCs with a low $\phi_{\rm M2}$ than binary PNCs without the compatibilizer, as seen in experiments.

Upon increasing the grafted filler fraction to $\phi_{PGP} = 0.079$ (Figure 9d-f), we find similar trends as those highlighted so far with $\phi_{PGP} = 0.039$ (Figure 9a-c). Particularly, at higher temperatures with increasing loadings of matrix_2 chains (Figure 9f and Figure S15f), the grafted nanoparticles are more dispersed than the binary PNC with $\phi_{M2} = 0$.

Taken together, the results in Figure 9 suggest that, at low temperatures (below the experimental LCST), the miscibility in ternary PNCs composed of chemically dissimilar graft (PMMA) and majority matrix (SAN) polymers with a small amount of compatibilizer (chemically identical matrix (PMMA)) is greater than in binary PNCs with no compatibilizer. This confirms the role of the PMMA chains in the ternary PNCs in stabilizing the interface between graft and matrix chains. We note that, at elevated temperatures above the LCST for PMMA/SAN (or due to the generality of the model, at temperatures below the UCST for a UCST graft-matrix system), the PNC miscibility in ternary PNCs composed of chemically dissimilar graft and majority matrix polymers with a small amount of chemically identical matrix is lower than in a binary PNC with chemically identical and chain length matched graft and matrix polymers.

Lastly, we confirm that, despite the differences between binary and ternary PNCs in the particle-particle correlations elucidated by the $g_{pp}(r)$ in Figure 9, as seen in experiments at high temperatures (Figures 2 and 3), we do not see major differences in the macroscale morphologies within the binary and ternary PNC with a low $\phi_{\rm M2}$ (Figure 10). The only differences we see between the binary and ternary PNCs at a low ϕ_{M2} are at a high $\varepsilon_{\mathrm{GM1}}$ of 0.2 kT; for example, in Figure 10a, $S_{\rm PP}({f q}
ightarrow 0)$ increases with increasing $\phi_{\rm M2}$ (also seen in Figure S16a). The binary PNC containing only PMMA chains $(\phi_{
m M2} pprox 1)$ exhibits a slight upturn at a low q and has the largest $S_{PP}(\mathbf{q} \to 0)$ magnitude. This suggests that, at high values of $\varepsilon_{
m GM1}$, the favorable enthalpic interactions between graft and matrix 1 chains in both binary and ternary PNCs serve to better disperse the NPs than the purely entropic forces between graft and matrix_2 chains. At $\varepsilon_{\rm GM1}$ = 0.07 kT (Figure 10c), binary and ternary PNCs with $\phi_{\rm M2}$ = 0-0.1 all show a significant upturn as $\boldsymbol{q} \to \boldsymbol{0},$ which reflects NP aggregation.

Overall, results from PRISM theory and MD simulations support the experimental observations that small amounts of matrix_2 (PMMA) chains serve as interfacial compatibilizers between the PMMA graft and long matrix_1 (SAN) chains at high temperatures. This interfacial compatibilization reduces the particle—particle correlation within aggregates likely explaining the reduction in cluster sizes of the nanoparticles at high temperatures.

CONCLUSIONS

In this study, binary and ternary phase diagrams were experimentally mapped using a combination of cloud point

observations, TEM, and SAXS for PMMA-NP/SAN and PMMA-NP/SAN/PMMA composites, respectively. When compared, they illustrate that the addition of a ternary component, namely, PMMA homopolymer to the binary PMMA-NP/SAN composite, results in an increased miscibility window at low loadings of grafted nanoparticles. The improved miscibility from the added homopolymer can be understood as a result of an interfacial compatibilization between the SAN matrix and grafted PMMA brush due to the PMMA homopolymer localization. A simple geometric model is presented, which predicts the extent of homopolymer compatibilization based on the relative loadings of each constituent. In addition, using PRISM theory calculations and MD simulations, the compatibilization effect of the added PMMA chains is systematically probed and compared to the experimental results. Importantly, MD simulations confirm the role of the PMMA chains in stabilizing the interface between graft and matrix chains in ternary PNCs. Additionally, PRISM theory results predict that the extent of compatibilization can be further tuned by varying the composition of the ternary PNCs. The generality of this compatibilization effect should apply to any PNC where the compatibilizer wets the grafted nanoparticle such that it reduces the interfacial energy between the binary constituents. Further, we hope that these results motivate further experimental and theoretical studies aimed at exploring the entire parameter space (i.e., molecular weight, grafting density, composition, etc.) in ternary nanocomposites to determine the parameters that yield the greatest improvement in miscibility. This study serves as a guideline to facilitate PNC miscibility at elevated temperatures, which is a critical parameter in designing technological applications, such as organic devices, that operate at high temperatures.

ASSOCIATED CONTENT

Supporting Information

The Supporting Information is available free of charge at https://pubs.acs.org/doi/10.1021/acs.macromol.0c02345.

Characterization of PNC constituents, sample preparation for ultramicrotomy, as-cast PNC characterization, cloud point images, TEM images of the PNCs annealed at longer times, discussion of SAXS model fitting, SAXS profiles at different NP loadings, simulation/theory parameters, brush height profiles, concentration profiles for SAN matrix at different interaction strengths, additional concentration profiles for PMMA graft and PMMA matrix chains at different loadings of PMMA matrix, additional $g_{\rm PP}(r)$ and $S_{\rm PP}({\bf q})$ at different loadings of PMMA matrix, and $S_{\rm GG}({\bf q})$ for PNCs at different compositions (PDF)

AUTHOR INFORMATION

Corresponding Authors

Arthi Jayaraman — Department of Chemical and Biomolecular Engineering, University of Delaware, Newark, Delaware 19716, United States; orcid.org/0000-0002-5295-4581; Email: arthij@udel.edu

Russell J. Composto – Department of Materials Science and Engineering, University of Pennsylvania, Philadelphia, Pennsylvania 19104, United States; oorcid.org/0000-0002-5906-2594; Email: composto@seas.upenn.edu

Authors

- Shawn M. Maguire Department of Materials Science and Engineering, University of Pennsylvania, Philadelphia, Pennsylvania 19104, United States
- Nadia M. Krook DuPont Co., Wilmington, Delaware 19803, United States; orcid.org/0000-0003-3308-9040
- Arjita Kulshreshtha Department of Chemical and Biomolecular Engineering, University of Delaware, Newark, Delaware 19716, United States
- Connor R. Bilchak Department of Materials Science and Engineering, University of Pennsylvania, Philadelphia, Pennsylvania 19104, United States; orcid.org/0000-0001-8815-1601
- Robert Brosnan Department of Materials Science and Engineering, University of Pennsylvania, Philadelphia, Pennsylvania 19104, United States
- Andreea-Maria Pana Department of Chemical and Biomolecular Engineering, University of Pennsylvania, Philadelphia, Pennsylvania 19104, United States
- Patrice Rannou Univ. Grenoble Alpes, CNRS, CEA, INAC-SyMMES, 38000 Grenoble, France; orcid.org/0000-0001-9376-7136
- Manuel Maréchal Univ. Grenoble Alpes, CNRS, CEA, INAC-SyMMES, 38000 Grenoble, France
- Kohji Ohno Department of Polymer Chemistry, Kyoto University, Kyoto 611-0011, Japan; ⊙ orcid.org/0000-0002-1812-3354

Complete contact information is available at: https://pubs.acs.org/10.1021/acs.macromol.0c02345

Author Contributions

[#]S.M.M. and N.M.K. contributed equally to this work.

Notes

The authors declare no competing financial interest.

ACKNOWLEDGMENTS

S.M.M., N.M.K., C.R.B., and R.J.C. were supported by the National Science Foundation Partnerships for International Research and Education Program (NSF-PIRE), grant #1545884. This research was additionally supported by the POLYMERS-DMR1905912 (S.M.M., N.M.K., C.R.B., and R.J.C.) and MRSEC-DMR-1720530 (S.M.M., N.M.K., C.R.B., and R.J.C.) programs. S.M.M., M.M., and P.R. also acknowledge support from the Centre National de la Recherche Scientifique (CNRS) at the laboratory of "Systèmes Moléculaires et nanoMatériaux pour l'Énergie et la Santé", (UMR5819-SyMMES (CNRS/CEA/Univ. Grenoble Alpes), Grenoble, France) and funding from the Agence Nationale de la Recherche (ANR): ANR-15- PIRE-0001-01 and ANR-15-PIRE-0001-07. The authors acknowledge use of the Duel Source and Environmental X-ray Scattering facility operated by the Laboratory for Research on the structure of Matter at the University of Pennsylvania (NSF MRSEC 17-20530). The equipment purchase was made possible by a NSF MRI grant (17-25969), an ARO DURIP grant (W911NF-17-1-0282), and the University of Pennsylvania. We thank Dr. Karen I. Winey and Dr. Christopher B. Murray for use of their laboratory's ultramicrotome and TEM, respectively. A.K. and A.J. acknowledge funding from the U.S. Department of Energy, Office of Science Grant (DE-SC0017753) and the use of Informational Technologies (IT) resources at the University of Delaware, including the high-performance computing resources of the

Farber and Caviness supercomputing clusters. The authors also acknowledge Dr. Robert A. Riggleman and Dr. Daeyeon Lee for helpful discussions.

REFERENCES

- (1) Glynos, E.; Papoutsakis, L.; Pan, W.; Giannelis, E. P.; Nega, A. D.; Mygiakis, E.; Sakellariou, G.; Anastasiadis, S. H. Nanostructured Polymer Particles as Additives for High Conductivity, High Modulus Solid Polymer Electrolytes. *Macromolecules* **2017**, *50*, 4699–4706.
- (2) Glynos, E.; Petropoulou, P.; Mygiakis, E.; Nega, A. D.; Pan, W.; Papoutsakis, L.; Giannelis, E. P.; Sakellariou, G.; Anastasiadis, S. H. Leveraging Molecular Architecture to Design New, All-Polymer Solid Electrolytes with Simultaneous Enhancement in Modulus and Ionic Conductivity. *Macromolecules* **2018**, *51*, 2542–2550.
- (3) Maréchal, M.; Niepceron, F.; Gebel, G.; Mendil-Jakani, H.; Galiano, H. Inside the Structure of a Nanocomposite Electrolyte Membrane: How Hybrid Particles Get along with the Polymer Matrix. *Nanoscale* **2015**, *7*, 3077–3087.
- (4) Hore, M. J. A.; Composto, R. J. Nanorod Self-Assembly for Tuning Optical Absorption. ACS Nano 2010, 4, 6941–6949.
- (5) Hore, M. J. A.; Composto, R. J. Functional Polymer Nanocomposites Enhanced by Nanorods. *Macromolecules* **2014**, 47, 875–887.
- (6) Ferrier, R. C., Jr.; Lee, H. S.; Hore, M. J. A.; Caporizzo, M.; Eckmann, D. M.; Composto, R. J. Gold Nanorod Linking to Control Plasmonic Properties in Solution and Polymer Nanocomposites. *Langmuir* **2014**, *30*, 1906–1914.
- (7) Bilchak, C. R.; Buenning, E.; Asai, M.; Zhang, K.; Durning, C. J.; Kumar, S. K.; Huang, Y.; Benicewicz, B. C.; Gidley, D. W.; Cheng, S.; Sokolov, A. P.; Minelli, M.; Doghieri, F. Polymer-Grafted Nanoparticle Membranes with Controllable Free Volume. *Macromolecules* **2017**, *50*, 7111–7120.
- (8) Ginzburg, V. V. Influence of Nanoparticles on Miscibility of Polymer Blends A Simple Theory. *Macromolecules* **2005**, *38*, 2362–2367.
- (9) Ferrier, R. C., Jr.; Koski, J.; Riggleman, R. A.; Composto, R. J. Engineering the Assembly of Gold Nanorods in Polymer Matrices. *Macromolecules* **2016**, *49*, 1002–1015.
- (10) Krook, N. M.; Ford, J.; Maréchal, M.; Rannou, P.; Meth, J. S.; Murray, C. B.; Composto, R. J. Alignment of Nanoplates in Lamellar Diblock Copolymer Domains and the effect of particle volume fraction on phase behavior. *ACS Macro Lett.* **2018**, 7, 1400–1407.
- (11) Rasin, B.; Chao, H.; Jiang, G.; Wang, D.; Riggleman, R. A.; Composto, R. J. Dispersion and Alignment of Nanorods in Cylindrical Block Copolymer Thin Films. *Soft Matter* **2016**, *12*, 2177–2185.
- (12) Schmitt, M.; Zhang, J.; Lee, J.; Lee, B.; Ning, X.; Zhang, R.; Karim, A.; Davis, R. F.; Matyjaszewski, K.; Bockstaller, M. R. Polymer Ligand—Induced Autonomous Sorting and Reversible Phase Separation in Binary Particle Blends. *Sci. Adv.* **2016**, *2*, No. e1601484.
- (13) Zhang, R.; Lee, B.; Bockstaller, M. R.; Kumar, S. K.; Stafford, C. M.; Douglas, J. F.; Raghavan, D.; Karim, A. Pattern-Directed Phase Separation of Polymer-Grafted Nanoparticles in a Homopolymer Matrix. *Macromolecules* **2016**, *49*, 3965–3974.
- (14) Higashida, N.; Kressler, J.; Inoue, T. Lower critical solution temperature and upper critical solution temperature phase behaviour in random copolymer blends: poly(styrene-co-acrylonitrile)/poly(methyl methacrylate) and poly(styrene-co-acrylonitrile)/poly(ε -caprolactone). *Polymer* 1995, 36, 2761–2764.
- (15) Suess, M.; Kressler, J.; Kammer, H. W. The Miscibility Window of Poly(Methyl Methacrylate)/Poly(Styrene-Co-Acrylnitrile) Blends. *Polymer* **1987**, *28*, 957–960.
- (16) Cowie, J. M. G.; Reid, V. M. C.; McEwen, I. J. Prediction of the Miscibility Range in Blends of Poly(Styrene-Co-Acrylonitrile) and Poly(N-Phenyl Itaconimide-Co-Methyl Methacrylate): A Six-Interaction-Parameter System. *Polymer* **1990**, *31*, 486–489.
- (17) Nishimoto, M.; Keskkula, H.; Paul, D. Miscibility of Blends of Polymers Based on Styrene, Acrylonitrile and Methyl Methacrylate. *Polymer* **1989**, *30*, 1279–1286.

- (18) Fowler, M. E.; Barlow, J. W.; Paul, D. R. Effect of Copolymer Composition on the Miscibility of Blends of Styrene-acrylonitrile Copolymers with Poly(Methyl Methacrylate). *Polymer* **1986**, *28*, 1177–1184.
- (19) Gao, J.; Huang, C.; Wang, N.; Yu, W.; Zhou, C. Phase Separation of Poly(Methyl Methacrylate)/Poly(Styrene-Co-Acrylonitrile) Blends in the Presence of Silica Nanoparticles. *Polymer* **2012**, 53, 1772–1782.
- (20) Gam, S.; Corlu, A.; Chung, H.-J.; Ohno, K.; Hore, M. J. A.; Composto, R. J. A Jamming Morphology Map of Polymer Blend Nanocomposite Films. *Soft Matter* **2011**, *7*, 7262–7268.
- (21) Chung, H. J.; Kim, J.; Ohno, K.; Composto, R. J. Controlling the Location of Nanoparticles in Polymer Blends by Tuning the Length and End Group of Polymer Brushes. *ACS Macro Lett.* **2012**, *1*, 252–256
- (22) Chung, H. J.; Ohno, K.; Fukuda, T.; Composto, R. J. Self-Regulated Structures in Nanocomposites by Directed Nanoparticle Assembly. *Nano Lett.* **2005**, *5*, 1878–1882.
- (23) Li, W. Effect of Silica Nanoparticles on the Morphology of Polymer Blends. *Technische Universiteit Eindhoven*; 2011, 1–159, DOI: 10.6100/IR719366.
- (24) Ojha, S.; Dang, A.; Hui, C. M.; Mahoney, C.; Matyjaszewski, K.; Bockstaller, M. R. Strategies for the Synthesis of Thermoplastic Polymer Nanocomposite Materials with High Inorganic Filling Fraction. *Langmuir* **2013**, *29*, 8989–8996.
- (25) Martin, T. B.; Mongcopa, K. I. S.; Ashkar, R.; Butler, P.; Krishnamoorti, R.; Jayaraman, A. Wetting—Dewetting and Dispersion—Aggregation Transitions Are Distinct for Polymer Grafted Nanoparticles in Chemically Dissimilar Polymer Matrix. *J. Am. Chem. Soc.* 2015, 137, 10624—10631.
- (26) Ohno, K.; Morinaga, T.; Koh, K.; Tsujii, Y.; Fukuda, T. Synthesis of Monodisperse Silica Particles Coated with Well-Defined, High-Density Polymer Brushes by Surface-Initiated Atom Transfer Radical Polymerization. *Macromolecules* **2005**, *38*, 2137–2142.
- (27) Grest, G. S.; Kremer, K. Molecular Dynamics Simulation for Polymers in the Presence of a Heat Bath. *Phys. Rev. A* **1986**, 33, 3628.
- (28) Jones, J. E. On the Determination of Molecular Fields. —II. From the Equation of State of a Gas. *Proc. R. Soc. London, Ser A* **1924**, *106*, 463–477.
- (29) Weeks, J. D.; Chandler, D.; Andersen, H. C. Role of Repulsive Forces in Determining the Equilibrium Structure of Simple Liquids. *J. Chem. Phys.* **1971**, *54*, 5237–5247.
- (30) Plimpton, S. Fast Parallel Algorithms for Short-Range Molecular Dynamics. *J. Comput. Phys.* **1995**, *117*, 1–19.
- (31) Nosé, S. A Molecular Dynamics Method for Simulations in the Canonical Ensemble. *Mol. Phys.* **1984**, *52*, 255–268.
- (32) Hoover, W. G. Canonical Dynamics: Equilibrium Phase-Space Distributions. *Phys. Rev. A* **1985**, *31*, 1695.
- (33) Schweizer, K. S.; Curro, J. G. PRISM Theory of the Structure, Thermodynamics, and Phase Transitions of Polymer Liquids and Alloys. In *Atomistic Modeling of Physical Properties*; Monnerie, L., Suter, U. W., Eds.; Springer: Berlin, 1994; Vol. 116, pp. 319–377.
- (34) Schweizer, K. S.; Curro, J. G. Integral-Equation Theory of the Structure of Polymer Melts. *Phys. Rev. Lett.* **198**7, *58*, 246.
- (35) Schweizer, K. S.; Curro, J. G. Integral Equation Theories of the Structure, Thermodynamics, and Phase Transitions of Polymer Fluids. *Adv. Chem. Phys.* **1997**, *98*, 1–142.
- (36) Ornstein, L. S.; Zernike, F. Accidental Deviations of Density and Opalescence at the Critical Point of a Single Substance. *Proc. Akad. Sci.* **1914**, *17*, 793–806.
- (37) Hansen, J.-P.; McDonald, I. R. *Theory of Simple Liquids*; 2nd ed.; Academic Press: London, 1986.
- (38) Hooper, J. B.; Schweizer, K. S. Theory of Phase Separation in Polymer Nanocomposites. *Macromolecules* **2006**, *39*, 5133–5142.
- (39) Hooper, J. B.; Schweizer, K. S.; Desai, T. G.; Koshy, R.; Keblinski, P. Structure, Surface Excess and Effective Interactions in Polymer Nanocomposite Melts and Concentrated Solutions. *J. Chem. Phys.* **2004**, *121*, 6986–6997.

- (40) Chandler, D.; Andersen, H. C. Optimized Cluster Expansions for Classical Fluids. II. Theory of Molecular Liquids. *J. Chem. Phys.* **1972**, *57*, 1930–1937.
- (41) Martin, T. B.; Gartner, T. E., III; Jones, R. L.; Snyder, C. R.; Jayaraman, A. PyPRISM: A Computational Tool for Liquid-State Theory Calculations of Macromolecular Materials. *Macromolecules* **2018**, *51*, 2906–2922.
- (42) Gam, S.; Meth, J. S.; Zane, S. G.; Chi, C.; Wood, B. A.; Seitz, M. E.; Winey, K. I.; Clarke, N.; Composto, R. J. Macromolecular Diffusion in a Crowded Polymer Nanocomposite. *Macromolecules* **2011**, *44*, 3494–3501.
- (43) Meth, J. S.; Zane, S. G.; Chi, C.; Londono, J. D.; Wood, B. A.; Cotts, P.; Keating, M.; Guise, W.; Weigand, S. Development of Filler Structure in Colloidal Silica-Polymer Nanocomposites. *Macromolecules* **2011**, *44*, 8301–8313.
- (44) Newby, B. Z.; Composto, R. J. Influence of Lateral Confinement on Phase Separation in Thin Film Polymer Blends. *Macromolecules* **2000**, *33*, 3274–3282.
- (45) Akcora, P.; Kumar, S. K.; Sakai, V. C.; Li, Y.; Benicewicz, B. C.; Schadler, L. S. Segmental Dynamics in PMMA-Grafted Nanoparticle Composites. *Macromolecules* **2010**, *43*, 8275–8281.
- (46) Akcora, P.; Liu, H.; Kumar, S. K.; Moll, J.; Li, Y.; Benicewicz, B. C.; Schadler, L. S.; Acehan, D.; Panagiotopoulos, A. Z.; Pryamitsyn, V.; Ganesan, V.; Ilavsky, J.; Thiyagarajan, P.; Colby, R. H.; Douglas, J. F. Anisotropic Self-Assembly of Spherical Polymer-Grafted Nanoparticles. *Nat. Mater.* **2009**, *8*, 354–359.
- (47) Chung, H.; Wang, H.; Composto, R. J. A Morphology Map Based on Phase Evolution in Polymer Blend Films. *Macromolecules* **2006**, *39*, 153–161.
- (48) Roe, R.-J.; Lu, L. Effect of Polydispersity on the Cloud-Point Curves of Polymer Mixtures. *J. Polym. Sci., Part B: Polym. Phys.* **1985**, 23, 917–924.
- (49) Rubinstein, M.; Colby, R. H. Polymer Physics; Oxford University Press, Oxford, UK, 2003.
- (50) Martin, T. B.; Jayaraman, A. Effect of Matrix Bidispersity on the Morphology of Polymer-grafted Nanoparticle-filled Polymer Nanocomposites. J. Polym. Sci. Part B Polym. Phys. 2014, 52, 1661–1668.